



35 (NACC), which became the next operational NAQFC system (i.e., NACC-CMAQ) on July
36 20, 2021. NACC-CMAQ has a number of scientific advancements that include satellite-
37 based data acquisition technology to improve land cover and soil characteristics, and inline
38 wildfire smoke and dust predictions that are vital to predictions of fine particulate matter
39 ($PM_{2.5}$) concentrations during hazardous events affecting society, ecosystems, and human
40 health. The GFS-driven NACC-CMAQ has significantly different meteorological and
41 chemical predictions than the previous operational NAQFC, where evaluation of NACC-
42 CMAQ shows generally improved near-surface ozone and $PM_{2.5}$ predictions and diurnal
43 patterns, both of which are extended to a 72-hour (3-day) forecast with this system.

44
45
46
47
48
49
50
51
52
53
54
55
56
57



58 **1. Introduction**

59

60 Air quality is defined as the degree in which the ambient air is free of pollutants--which are
61 either directly emitted into the atmosphere (primary air pollutants) or formed within the
62 atmosphere itself (secondary air pollutants)--that cause degradation to human health, visibility,
63 and/or ecological systems (WHO, 2005). Air quality is as ubiquitous and important as weather
64 impacts, where outdoor air pollution is responsible for ~4.2 million early deaths globally each
65 year (https://www.who.int/health-topics/air-pollution#tab=tab_1). To put this into perspective:
66 this is over three times the number of people who die from HIV/AIDS and over eight times the
67 number of homicides each year (2017 Global Burden of Disease Study:
68 <https://www.thelancet.com/gbd>). Air pollution is costly, and leads to huge economic damage
69 (Landrigan et al., 2018). There are also disproportionate impacts of air pollution across poorer
70 people and some racial and ethnic groups, who are among those who often face higher exposure
71 and potential responses to pollutants (Institute of Medicine, 1999; American Lung Association,
72 2001; O'Neil et al., 2003; Finkelstein et al., 2003; Zeka et al., 2006).

73 Air pollutants are composed of both gaseous and particulate species, which under prolonged
74 exposure can cause non-carcinogenic (Lee et al., 2014) and/or carcinogenic adverse health
75 effects (Demetirou and Vineis, 2015). High ground-level ozone (O₃) concentrations (i.e., smog)
76 for example, can lead to decreased lung function and cause respiratory symptoms. These
77 symptoms are particularly dangerous for sensitive groups such as young children, the elderly,
78 and those with preexisting conditions that include asthma, chronic obstructive pulmonary disease
79 (COPD), lung cancer, and respiratory infection (Kar Kurt et al., 2016).

80 To protect against the health and environmental impacts of air pollution, world agencies have
81 developed regulations and standards on the allowable amount of primary and secondary air



82 pollution measured at different spatiotemporal scales (e.g., seconds to months and local to global
83 scales), which largely depend on the atmospheric lifetime of specific air components (WHO,
84 2005, 2010). Typically, the world's most extreme air pollution occurs near global megacities
85 where population density is highest (Marlier et al., 2016). Rapid economic growth in China, for
86 example has led to extremely high air pollution levels over the past decade (Zhou et al., 2017;
87 Liu and Wang, 2020), necessitating significant efforts to implement air pollution prevention and
88 control plans (Chinese State Council, 2013; Zhao et al., 2014). The U.S. Environmental
89 Protection Agency (EPA) defines ambient concentration limits for primary pollutants such as
90 sulfur dioxide (SO₂), oxides of nitrogen (NO_x = NO+NO₂), carbon monoxide (CO), lead (Pb),
91 and total (carbonaceous and non-carbonaceous) particulate matter (PM). Other important
92 primary pollutants include total volatile organic compounds (VOCs), which have many sources
93 (both natural and anthropogenic) and serve as vital precursor gases to secondary pollutants such
94 as ground-level O₃ and the formation of fine particulate matter with an aerodynamic diameter of
95 less than 2.5 μm (PM_{2.5}). Ground level O₃ and PM_{2.5} are two of the six U.S. EPA “criteria
96 pollutants” that are regulated for their concentrations, exposure level, and health impacts. This is
97 largely because there is a relatively mature understanding of their sources, formation, and
98 characteristics (e.g., Sillman et al., 1990; Sillman 1995, 1999; Pinder et al., 2008; Kim et al.,
99 2011a, 2011b; Zhang et al., 2009a, 2009b; Campbell et al., 2015; Karamchandani, et al. 2017).
100 There is also a widespread ability to compare observed and simulated ambient ozone
101 concentrations over both short-term (McKeen et al., 2004, 2007, 2009) and dynamic long-term
102 periods (e.g., Astitha et al., 2017), which has helped lead to an understanding of their well-
103 attributable health impacts (e.g., WHO 2006, Sun et al., 2015; Zhang et al., 2018).



104 To address prolific air pollution concerns in the U.S. during the 1950s-1960s, the first
105 development and application of real-time air quality forecast (RT-AQF) models began in the
106 1970s-1980s (i.e., the 1st and 2nd generation air quality models) coincident with the
107 establishment of the U.S. EPA by President Nixon. Initially the models were based on empirical
108 approaches and statistical models (Zhang et al., 2012a); however, by the 1990s and early 2000s,
109 RT-AQF models underwent a significant evolution and evolved to more complex 3-D numerical
110 air quality models (3rd and 4th generation air quality models). These RT-AQF models involved
111 more sophisticated techniques including increasingly complex parameterizations and chemistry,
112 bias correction methods and data fusion, chemical data assimilation, and hybrid statistical or
113 numerical methods with artificial intelligence/machine learning algorithms to improve RT-AQF
114 model efficiency and predictions (Zhang et al., 2012b; Bai et al., 2018). RT-AQF models have
115 become vital tools to improve our understanding and prediction of how air pollutants form,
116 disperse, and deposit to the surface, and are used by local health and air managers to assess the
117 air quality conditions to make informed decisions on mitigation measures to reduce public
118 exposure.

119 To address the nation's need for reducing the adverse health effects of air pollution and
120 associated costly medical expenses, in 2002 Congress addressed the National Oceanic and
121 Atmospheric Administration (NOAA) to provide National AQF guidance (H.R. Energy Policy
122 Act of 2002 - Senate Amendment S. 517, SA1383, Forecasts and Warnings). A joint project
123 emerged from this amendment between NOAA and the EPA to develop and establish the initial
124 phase of a RT-AQF system, which consisted of the coupled NOAA's Eta meteorological model
125 (Black, 1994; Rogers et al., 1996) with EPA's Models-3 Community Multiscale Air Quality
126 (CMAQ) model (Byun and Ching, 1999; Byun and Schere, 2006). This "offline-coupled" model



127 provided O₃ forecast guidance for the northeastern U.S states (Kang et al., 2005; Otte et al.,
128 2005; Eder et al., 2006) and formed the early version of the National Air Quality Forecast
129 Capability (NAQFC) that was first implemented for operations in September 2004
130 (https://www.weather.gov/sti/stimodeling_airquality_predictions). The NAQFC was further
131 developed at NOAA and collaborating laboratories (Mathur et al., 2008; McKeen et al., 2004,
132 2007, 2009), and was comprehensively evaluated in Eder et al. (2009). The NAQFC has been
133 continuously advanced to provide both O₃ and PM_{2.5} forecast guidance for the entire
134 conterminous U.S. (CONUS), expanded its predictions to both Alaska and Hawaii, and provided
135 pivotal air quality forecast guidance to a multitude of stakeholders to help protect human health
136 and the environment (Stajner et al., 2011; Lee et al., 2017; Huang et al., 2017). Prior to the
137 advanced version described in this paper, the NAQFC used the offline-coupled North American
138 Mesoscale Model Forecast System on the B-Grid (NMMB) (Black, 1994; Janjic and Gall, 2012)
139 and CMAQv5.0.2 (U.S. EPA, 2014). The NAQFC provides forecast guidance for O₃, PM_{2.5},
140 wildfire smoke, and dust at a horizontal grid spacing of 12 km over a domain centered on the
141 CONUS, Alaska, and Hawaii domains.

142 NOAA's National Weather Service (NWS) transitioned operationally in June 2019 to use a
143 new dynamical core known as the Finite Volume Cubed-Sphere (FV3) in the Global Forecast
144 System (GFS) model. Both the National Aeronautics and Space Administration (NASA) and
145 NOAA's Geophysical Fluid Dynamics Laboratory (GFDL; <https://www.gfdl.noaa.gov/>) have
146 developed and advanced FV3 over the past few decades (Lin et al., 1994; Lin and Rood, 1996;
147 Lin, 2004; Putman and Lin, 2007; Chen et al., 2013; Harris and Lin, 2013; Harris et al., 2016;
148 Zhou et al., 2019). Overall, the switch to a FV3-based dynamical core with advancements to
149 GFS's observation quality control, data assimilation, and model physical parameterizations (from



150 the National Center for Environmental Prediction) significantly increases the accuracy of 1-2 day
151 and longer (e.g., 3-7 day) weather forecasts (Chen et al., 2018). Other advantages of FV3GFS
152 are improved computational efficiency and adaptable scaling, enhanced and flexible vertical
153 resolution, and improved representation of atmospheric circulation and weather patterns across
154 different horizontal scales (Yang et al., 2020);
155 https://www.weather.gov/media/notification/pns20-44gfs_v16.pdf;
156 https://www.emc.ncep.noaa.gov/emc/pages/numerical_forecast_systems/gfs.php;
157 [https://ufsccommunity.org/wp-](https://ufsccommunity.org/wp-content/uploads/2020/10/UFS_Webnair_GFSv16_20201022_FanglinYang.pdf)
158 [content/uploads/2020/10/UFS_Webnair_GFSv16_20201022_FanglinYang.pdf](https://ufsccommunity.org/wp-content/uploads/2020/10/UFS_Webnair_GFSv16_20201022_FanglinYang.pdf)).

159 The improved representation of atmospheric conditions, circulation/transport, and
160 precipitation in GFS are pivotal to the accuracy of chemical predictions when coupled to RT-
161 AQF models. Since 2017, there also has been significant efforts at NOAA to use version 15 of
162 FV3GFS (hereafter, GFSv15) rather than NMMB as the meteorological driver for CMAQ in the
163 NAQFC (Huang et al., 2018, 2019, 2020). Huang et al. (2020) and Chen et al. (2021)
164 demonstrated that a version of the GFS-driven CMAQv5.0.2 (GFSv15-CMAQ) forecasting
165 system had improved O₃ predictions compared to the NMMB-driven CMAQ (NMMB-CMAQ)
166 system, but that the GFSv15-CMAQ had large biases for PM_{2.5} that still need improvement.

167 Concurrently at NOAA, there is a major upgrade of GFS from version 15 to 16 (GFSv16),
168 which includes a number of major developmental advances to the system (see Section 2 of this
169 paper). Thus, there was an opportunity to simultaneously upgrade and streamline the
170 meteorological coupling between the GFSv16 and a more updated, “state-of-the-science” version
171 of CMAQ at the U.S. EPA (U.S. EPA, 2019; Appel et al., 2021). The current CMAQv5.0.2 used
172 in the NMMB-CMAQ and experimental GFSv15-CMAQ is outdated scientifically with



173 numerous deficiencies, many of which led to the elevated biases and error as described in Huang
174 et al. (2017; 2020) and Chen et al. (2021). Hence, there is a need to update the NAQFC to
175 actively developing versions of both FV3GFS and CMAQ.

176 The main objectives of this manuscript are to describe the development of the GFSv16
177 coupling with a state-of-the-science CMAQ model for the advanced updates to NAQFC that
178 includes numerous other RT-AQF science advances (Section 2). We also describe the new
179 simulation design and input observations, and evaluate the meteorological and air quality
180 predictions across the U.S. compared to the now discontinued NMMB-CMAQ system for
181 NAQFC (Sections 3 and 4). We conclude with a summary of NACC-CMAQ serving as the
182 current (since July 20, 2021) operational NAQFC, as well as longer-term goals (Section 5). We
183 hypothesize that advancing to closer state-of-the-science meteorological and chemical transport
184 models will improve atmospheric-chemical composition predictions, and the resulting air quality
185 forecasts will better protect human health across the U.S. Tang et al. (2021b) provides more
186 details and evaluations of the individual scientific advancements for different air quality cases
187 (including windblown dust and wildfire smoke events), as well as further assessment of the new
188 system to be used for community research applications.

189 **2. Methods**

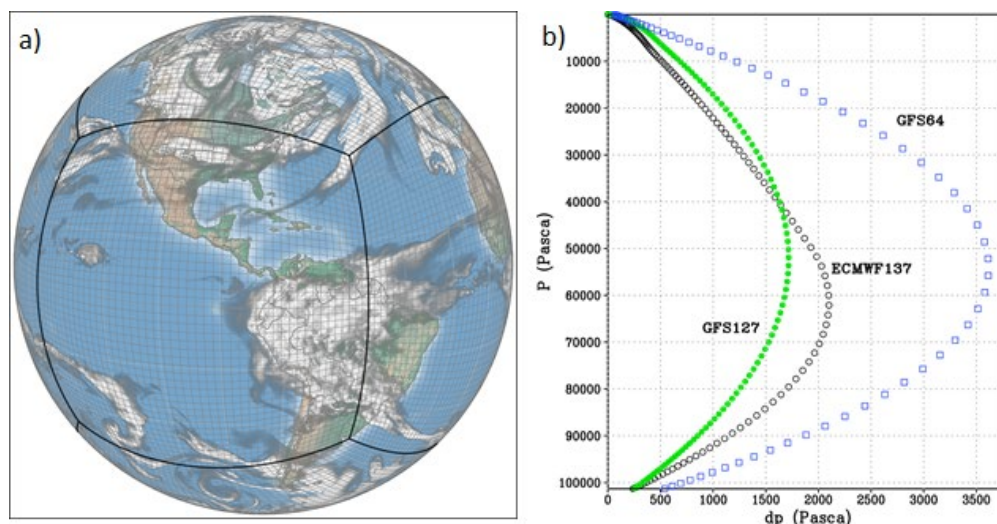
190 191 2.1 Updated Meteorological and Surface Drivers

192 193 2.1.1 *The Global Forecast System Version 16*

194 The Environmental Modeling Center (EMC) at NOAA continuously develops and
195 improves the GFS model, which has been in operation at the National Weather Service since
196 1980. EMC has recently upgraded the GFS model from v15.3 to v16 in February 2021, and the
197 major upgrade improves the model forecast performance while also providing enhanced forecast
198



199 products. Some of the major structural changes to GFSv16 (compared to previous GFS versions)
200 include increased vertical layers/resolution from 64 to 127 (Figure 1) and an extended model top
201 from 54 (upper stratosphere) to 80 km (mesopause). GFSv16 also has a thinner first model layer
202 thickness (20 m) and higher resolution global horizontal grids of ~ 25 and 13 km (Yang et al.,
203 2020; https://www.weather.gov/media/notification/pns20-44gfs_v16.pdf;
204 https://www.emc.ncep.noaa.gov/emc/pages/numerical_forecast_systems/gfs.php;
205 [https://ufsccommunity.org/wp-](https://ufsccommunity.org/wp-content/uploads/2020/10/UFS_Webnair_GFSv16_20201022_FanglinYang.pdf)
206 [content/uploads/2020/10/UFS_Webnair_GFSv16_20201022_FanglinYang.pdf](https://ufsccommunity.org/wp-content/uploads/2020/10/UFS_Webnair_GFSv16_20201022_FanglinYang.pdf)).



208 **Figure 1.** The a) native FV3 gnomonic cubed-sphere grid at C48 (2-degree) resolution (image
209 courtesy of Dusan Jovic, NOAA) and b) vertical resolution (P vs. dP) for the upgraded GFSv16
210 (green) compared to the previous GFSv15.3 (blue) and the European Centre for Medium-Range
211 Weather Forecasts (ECMWF) model (black).

212
213
214

The GFSv16 has significantly improved its physical parameterizations (e.g., Planetary
215 Boundary Layer (PBL), gravity wave, radiation, clouds and precipitation, land surface, and
216 surface layer schemes) and upgraded to the Global Data Assimilation System (GDAS) Version
217 16 (Yang et al., 2020; https://www.weather.gov/media/notification/pns20-44gfs_v16.pdf;



218 https://www.emc.ncep.noaa.gov/emc/pages/numerical_forecast_systems/gfs.php;
219 [https://ufsccommunity.org/wp-](https://ufsccommunity.org/wp-content/uploads/2020/10/UFS_Webnair_GFSv16_20201022_FanglinYang.pdf)
220 [content/uploads/2020/10/UFS_Webnair_GFSv16_20201022_FanglinYang.pdf](https://ufsccommunity.org/wp-content/uploads/2020/10/UFS_Webnair_GFSv16_20201022_FanglinYang.pdf)).

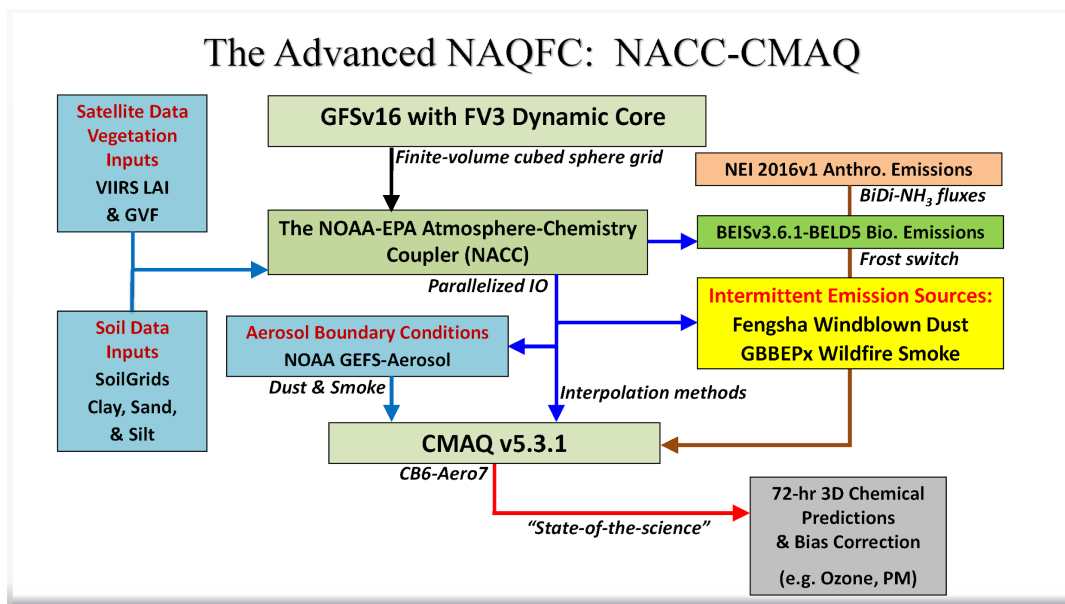
221 The global GFSv16 has changed format of forecast output history files from binary
222 (nemsio) to netCDF with zlib compression (data volume reduced by about 60%), and provides
223 the *hourly* (important for CMAQ predictions) output for a 72-hour (3-day) forecast each day.
224 The prior operational NAQFC (NMMB-CMAQ) forecast is only out to 48 hours (2-day). The
225 netCDF output is available (via live disk and archives) to all of NOAA’s downstream model
226 applications, and is in the form of a Gaussian, rectangular grid with a global-uniform grid
227 resolution of ~13 km (referred to as “C768”), with a set number of latitude and longitude
228 coordinates. The NOAA GFDL website provides more information about FV3 and its grids
229 (<https://www.gfdl.noaa.gov/fv3/>). There are additional new surface fields in the GFSv16 output,
230 which include plant canopy surface water, surface temperature and moisture at four below-
231 ground levels (0-0.1, 0.1-0.4, 0.4-1, 1-2 m), surface roughness, soil and vegetation type, and
232 friction velocity.

233 2.1.2 The NOAA-EPA Atmosphere Chemistry Coupler (NACC)

234
235 The meteorological-chemical coupling of the GFSv16 to the regional, state-of-the-science
236 CMAQ v5.3.1 model (U.S. EPA, 2019; Appel et al., 2021) is achieved via the NOAA-EPA
237 Atmosphere Chemistry Coupler (NACC) version 1 (NACC, i.e., “*knack*”: meaning an acquired
238 *skill*), which is adapted from the U.S. EPA’s Meteorology-Chemistry Interface Processor (MCIP)
239 version 5 (Otte and Pleim, 2010; <https://github.com/USEPA/CMAQ>). The NACC and CMAQ
240 coupling (hereafter referred to as NACC-CMAQ) involves a number of structural and scientific



241 advancements (Figure 2; “The Advanced NAQFC”) compared to the previous operational
242 NMMB-CMAQ; hereafter referred to as “prior NAQFC”.



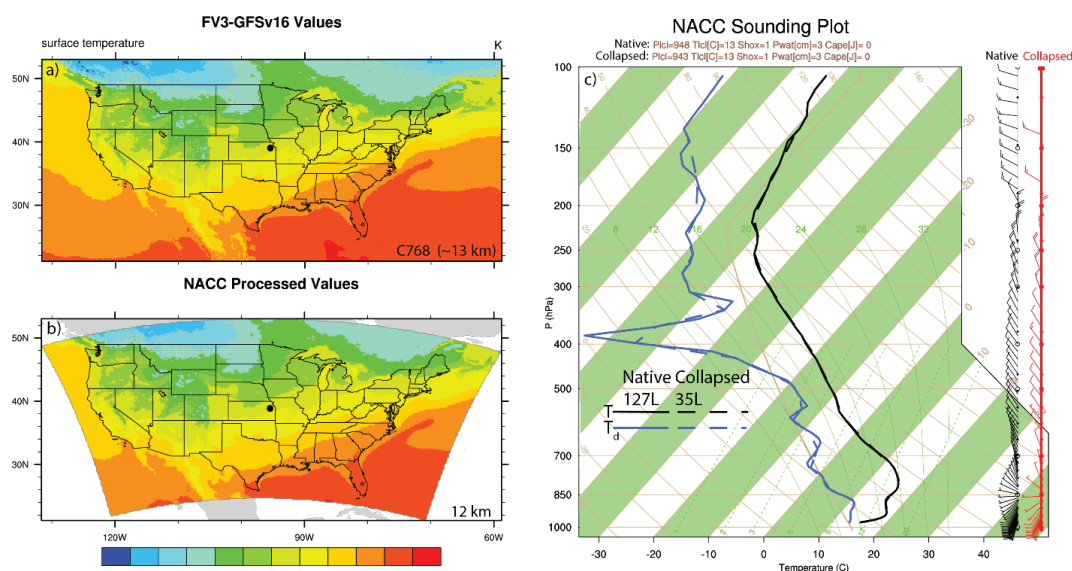
244 **Figure 2.** Schematic of the advanced NAQFC based on NACC-CMAQ.

245

246

247 The major structural changes to NACC-CMAQ include a variable-dependent bilinear or
248 nearest-neighbor horizontal interpolation of the GFSv16 Gaussian gridded (~13 km) fields (e.g.,
249 2-m temperature, 2-meter specific humidity, 10-m wind speed and direction, and sea level
250 pressure) to Lambert Conic Conformal (LCC) at 12-km horizontal grid spacing (same as the
251 prior NAQFC) (Figures 3a-b). NACC-CMAQ also includes a redefined vertical structure based
252 on vertical interpolation (i.e., collapsing) to a 35-layer configuration (Figure 3c) that is identical
253 to the prior NAQFC.

253



255 **Figure 3.** Examples of the NACC-CMAQ a) GFSv16 Gaussian grid surface temperature
256 (C768~13 km) and b) associated bilinear horizontal interpolation NACC LCC output (12 km),
257 and c) Skew-T Log-P diagram of both GFSv16 native (127 layers; solid) and NACC interpolated
258 (35 layers; dashed) profiles of temperature (black) and dewpoint (blue), and wind speed/direction
259 (wind barbs; native=black and collapsed=red). The example sounding pertains to a date of
260 September 24, 2020 at the closest model grid square to 39.07°N and 95.62°W (black dot in a-
261 b)).

262 Time-splitting techniques based on Message Passing Interface (MPI) commands
263 parallelize the GFSv16-to-NACC input and output (IO), which vastly improves the
264 computational efficiency for the updated 72-hr forecast period. The NACC-CMAQ coupling is
265 more unified and streamlined compared to prior NAQFC (Stajner et al., 2011; Lee et al., 2017;
266 Huang et al., 2017) and experimental GFSv15-CMAQ (Huang et al., 2018; 2019) applications,
267 while eliminating multiple pre- and post-processing steps. The NACC-CMAQ processing steps
268 are therefore subject to less uncertainty/error that comes with multiple grid interpolations and
269 restructuring used previously, and are more computationally efficient for the 72-hr forecast
270 window. Furthermore, the vertical interpolation from 127 to 35 layers results in an excellent
271 agreement in the vertical structure of key atmospheric state variables (Figure 3c). While this
272 example is only for the central U.S., other model grid cell locations in the east and west U.S. also



273 demonstrate excellent agreement in the native and collapsed vertical structure in NACC (not
274 shown). The NACC-CMAQ domains for Alaska and Hawaii remain under development, so this
275 paper focuses only on the results inside the CONUS domain.

276 The left side of Figure 2 shows that NACC-CMAQ incorporates high resolution satellite
277 data for a 2018-2020 climatological (12-month) averaged leaf area index (LAI), which is based
278 on the Visible Infrared Imager Radiometer Suite (VIIRS) 8-day, Level 4 Global 500 m SIN Grid,
279 V001 product (Myneni and Knyazikhin, 2018; <https://lpdaac.usgs.gov/products/vnp15a2hv001/>).
280 This is a substantial update from the prior NAQFC, which assumed an unrealistic static value of
281 LAI = 4 across the entire domain. The NOAA product for near-real-time (NRT) greenness
282 vegetation fraction (GVF) from VIIRS (Ding and Zhu, 2018;
283 <https://www.ospo.noaa.gov/Products/land/gvf/>) is used as a dynamic, direct input in NACC-
284 CMAQ instead of using the GFSv16 vegetation fraction (VEG). Both VIIRS LAI and GVF are
285 preprocessed, and NACC performs nearest-neighbor interpolation to the NAQFC grid.

286 More realistic land cover characteristics have shown to improve modeled meteorology,
287 chemistry, and surface-atmosphere exchange processes in the coupled Weather Research and
288 Forecasting (WRF; Powers et al., 2017; Skamarock & Klemp, 2008)-CMAQ model (e.g., Ran et
289 al., 2016; Campbell et al., 2019). Test results here show that rapid-refresh of high resolution
290 VIIRS LAI and GVF in NACC have distinct differences compared to an older 2010 MODIS-
291 International Geosphere-Biosphere Programme (IGBP) LAI climatology and GFSv16-based
292 VEG, respectively (Figs. S1-S2). The updated, dynamic LAI and GVF alter biogenic emissions,
293 dry deposition, and resulting concentrations of gases and aerosols in NACC-CMAQ, particularly
294 during the fall transition month of October 2020 (Fig. S3).



295 NACC-CMAQ also uses global, gridded soil information based on the 2019 SoilGrids™
296 250-m resolution data (<https://www.isric.org/explore/soilgrids>) to drive an inline FENGSHA
297 Windblown dust model (Fu et al., 2014; Huang et al., 2015; Dong et al., 2016) in NACC-CMAQ
298 (Figure 2). Section 2.2 below provides more information on the specific parameters used in
299 FENGSHA.

300 As in the operational NAQFC, a NRT bias-correction using AirNow surface observations
301 (<https://www.airnow.gov/>) is applied to the 72-hr predictions of O₃ and PM_{2.5} (Figure 2). Huang
302 et al. (2017) provides more information on the bias-correction technique.

303 2.2 Updated Chemistry, Emissions, and Air-Surface Exchange Processes

304

305 2.2.1 *The Community Multiscale Air Quality (CMAQ) Model, Version 5.3.1*

306

307 A major update in NACC-CMAQ is coupling the GFSv16 to a “state-of-the-science”
308 chemical transport model, CMAQv5.3.1 (U.S. EPA, 2019; Appel et al., 2021) (Figure 2). The
309 prior NAQFC and experimental GFSv15-CMAQ both use CMAQv5.0.2, released in April 2014
310 (U.S. EPA, 2014). The major release of CMAQv5.3 incorporates significant improvements to
311 gas chemistry (e.g., halogen-mediated ozone loss), aerosol modules (e.g., improved secondary
312 organic aerosol formation), photolysis rates, aqueous and heterogeneous chemistry, transport
313 processes, air-surface exchange, emissions, and other structural and computational improvements
314 (Appel et al., 2021). The use of CMAQv5.3.1 in NACC-CMAQ also contains a number of bug
315 fixes to v5.3. Version 6 of the Carbon Bond (CB6) mechanism is used for gas-phase chemistry
316 (Yarwood et al., 2010), and the updated U.S. EPA’s AERO7 module is used for aerosol
317 formation in NACC-CMAQ. The U.S. EPA’s GitHub webpage
318 (https://github.com/USEPA/CMAQ/blob/master/DOCS/Release_Notes/README.md) contains
319 the CMAQv5.3 and v5.3.1 release notes, mechanism descriptions, and enhancements.



320 *2.2.2 National Emissions Inventory Collaborative (NEIC) 2016v1 Emissions*
321
322 The anthropogenic emissions modeling data may be the most influential input for chemical
323 transport model predictions in any AQF system (Matthias et al., 2018). The model emissions are
324 updated from National Emissions Inventory (NEI) 2014 version 2 that is used by the prior
325 NAQFC to NEI Collaborative (NEIC) 2016v1 Emissions Modeling Platform (NEIC, 2019),
326 which is based on updated models and datasets applied to the U.S. Environmental Protection
327 Agency's (EPA) NEI2014v2. The prior NAQFC uses an older NEI2014v2 emissions dataset.
328 There have been substantial updates to the NEIC2016v1, which include emission decreases for
329 CO, NO_x, SO₂, and PM_{2.5}, and increases in total VOC and ammonia (NH₃) emissions compared
330 to the NEI2014v2 (NEIC, 2019). The intermittent, "event-based" emissions from wildfires and
331 windblown dust, as well as persistent biogenic emissions sources are not from the NEIC2016v1,
332 but rather are dynamically predicted inline within NACC-CMAQ (described in following
333 sections). The NEIC2016v1 area-source (i.e., 2-D) emissions are gridded, netCDF/IOAPI format
334 that are interpolated to the 12-km NAQFC domain. The NEIC2016v1 also provides major point
335 source (i.e., 3D) emissions from six sectors: Commercial Marine Vehicles (CMV12 and
336 CMV3), Electricity Generating Units (EGUs), Non-EGUs, Oil-Gas sources, and "Other" point
337 sources. The anthropogenic point source plume rise is calculated inline within NACC-CMAQ
338 using the Briggs plume rise method (Briggs, 1965). Slight adjustments are made to reduce the
339 anthropogenic aerosol/fugitive dust emissions over snow and wet soil surfaces to account for
340 different forecasted meteorology in GFSv16 compared to the conditions used in generating the
341 NEIC2016v1.

342 We note that the NEIC2016v1 emissions are not projected into the actual forecast year, with
343 the time lag being a long-recognized issue in NAQFC (e.g., Tong et al., 2012). Thus, the



344 NACC-CMAQ air quality simulations for the fall of 2020 and the winter of 2021 are impacted
345 by the COVID-19 pandemic, which resulted in significant changes to emission patterns and
346 ozone formation over the U.S. in 2020 and beyond (Campbell et al., 2021). In addition, mobile
347 source emissions have continued to decline since 2016 so it is likely that the emissions used in
348 the analysis do not entirely reflect recent changes to the emissions compared to 2016 (almost 5
349 years earlier). We are actively working to improve the representativeness of anthropogenic
350 emissions sources in NACC-CMAQ and next-generation versions of the NAQFC.

351 *2.2.3 Inline Biogenic Emissions and Bidirectional NH₃ Fluxes*

352 NACC-CMAQ uses the latest version of the Biogenic Emission Inventory System (BEIS)
353 v3.6.1 (Vukovich and Pierce, 2002; Schwede, 2005) for estimating the biogenic VOC (BVOC)
354 emissions. BEISv3.6.1 includes updated vegetation inputs and advanced two-layer canopy
355 model formulations for estimating leaf (sun and shade) temperatures and vegetation data (Weiss
356 and Norman, 1985; Campbell and Norman, 1998; Niinemets et al., 2010; Bash et al., 2015).
357 NACC-CMAQ also uses the revised Biogenic Emissions Landuse Dataset v5 (BELD5), which
358 includes a newer version of the Forest Inventory and Analysis (FIA) version 8.0 and updated
359 agricultural land use from the 2017 U.S. Department of Agriculture (USDA) crop data layer.
360 The BELD5 dataset also uses a MODIS 21-category land use dataset with lakes identified
361 separately from oceans. The prior NAQFC used a much older BELD3 version.

362 The prior NAQFC also only considered summer factors in BEIS, and did not capture
363 seasonal (summer and winter) changes to the normalized biogenic emissions factors (vegetation
364 species-specific). NACC-CMAQ is improved and uses a new “vegetation frost switch” that
365 adjusts between summer and winter normalized emission factors in BEISv3.6.1 based on the
366 calendar date and 2-m temperature (TEMP2). In NACC, a new time-dependent variable,



367 ‘SEASON’ is equal to one during the growing season, or equal to zero outside the growing
368 season. The SEASON is (boreal) summer if the calendar date is on or between 15 April and 15
369 October, but switches to winter if TEMP2 drops below 28°F, and is winter if the date is on or
370 between 16 October and 14 April, but switches to summer if TEMP2 rises above 32°F. Thus,
371 the SEASON variable in NACC-CMAQ differs from typical retrospective CMAQ applications,
372 and is more dynamic with hourly variability based on the GFSv16 forecasted TEMP2. Test
373 results show generally improved model performance for all U.S. regions in December 2020
374 (winter) with vegetation frost switch compared to using only summer season normalized
375 emissions (Table S1). Using BELD5 further improves model performance and reduces the error
376 in all CONUS regions compared to the older BELD3 used in December 2020 tests (Table S1).

377 NACC-CMAQ includes bidirectional NH₃ (BIDI-NH₃) for NH₃ fluxes (i.e., both
378 deposition and evasion) in the CMAQv5.3.1 “M3Dry” deposition model (Nemitz et al., 2000;
379 Cooter et al., 2010; Massad et al., 2010; Pleim and Ran, 2011; Bash et al., 2010, 2013; Pleim et
380 al., 2013; 2019). Here, the NH₃ fertilizer emissions are removed from the base NEIC2016v1
381 inventory to avoid double counting, as the inline BIDI-NH₃ module calculates these fluxes. The
382 BIDI-NH₃ module typically requires daily inputs (e.g., soil ammonia content, soil pH, soil
383 moisture, and other soil characteristics) from the USDA’s Environmental Policy Integrated
384 Climate (EPIC) agroecosystem model (<https://epicapex.tamu.edu/epic/>; Williams et al., 1995) to
385 calculate the soil ammonia concentrations that are combined with air concentrations in CMAQ to
386 calculate BIDI-NH₃ fluxes. Typically, the Fertilizer Emission Scenario Tool (FEST-C,
387 <https://www.cmascenter.org/fest-c/>) processes the necessary meteorological conditions for
388 integration with the EPIC simulation for input to CMAQ (Ran et al., 2011; Cooter et al., 2012).
389 Use of the EPIC/FEST-C system is not feasible in an NRT operational forecasting model, and



390 thus we use a pre-generated, full-year 2011 EPIC/FEST-C simulation based on Campbell et al.
391 (2019) for the daily inputs to BIDI-NH₃ in NACC-CMAQ. NACC-CMAQ directly uses the
392 GFSv16 soil moisture conditions in place of the FEST-C processed soil conditions required for
393 the latest version of BIDI-NH₃ in CMAQv5.3.1 (Pleim et al., 2019).

394 *2.2.4 Inline Wildfire Smoke and Windblown Dust Emissions*

395
396 Wildfires have been increasing in size (Westerling et al., 2006) and potentially in severity
397 (Miller et al., 2009) over the past decades. Wildfire smoke outbreaks can lead to extreme
398 concentrations of PM_{2.5} and enhanced O₃, and are major concerns for air quality forecasting and
399 consequential human and ecosystem health impacts. NACC-CMAQ includes a new inline
400 calculation of wildfire smoke emissions based on the Blended Global Biomass Burning
401 Emissions Product (GBBEPx V3; Zhang et al., 2012, 2014). GBBEPx provides hourly global
402 biomass burning emissions (PM_{2.5}, BC, OC, NO_x, NH₃, CO, and SO₂). It blends fire
403 observations from two sensors, including the Moderate Resolution Imaging Spectroradiometer
404 (MODIS) on the NASA Terra and Aqua satellites, and the Visible Infrared Imaging
405 Spectrometer (VIIRS) on the Suomi National Polar-orbiting Partnership (SNPP) and Joint Polar-
406 orbiting Satellite System 1 (JPSS1) satellites. The GBBEPx data are further processed to prepare
407 model-ready emission datasets. First, the 0.1 x 0.1 degree latitude/longitude data are converted
408 into the NAQFC LCC projection. U.S. EPA-based Sparse Matrix Operator Kernel Emissions
409 (SMOKE) fire speciation and diurnal profiles provide the PM speciation and diurnal patterns in
410 NACC-CMAQ, respectively, while both landuse and region are used to identify fire types. The
411 fire duration persists for the 72-hour forecast period (with scaling of 1.0, 0.25, and 0.25 for day
412 1, 2, and 3, respectively) for wildfires identified when the grid cell forest fraction is > 0.4. In the
413 eastern U.S. (longitude east of 100°W), however, the fires are assumed to be mainly prescribed



414 burns in forested regions that only persist for the first 24-hours. The wildfire plume rise is
415 calculated inline within NACC-CMAQ using either the Briggs (1965) or Sofiev et al. (2012)
416 algorithms (Wilkins et al. 2019); currently the Briggs method is used by default.

417 Climate models project warming and drying trends in the southwestern U.S., where
418 intermittent windblown dust storms are becoming more frequent with the occurrence of drought
419 (Tong et al., 2017), or even “megadrought” conditions (Williams et al., 2020). Windblown dust
420 storms can lead to extreme levels of coarse mode particulate matter (i.e., PM₁₀), and cause
421 detrimental effects to human and agroecosystem health and visibility. NACC-CMAQ includes a
422 novel inline methodology for calculating windblown dust, based on the FENGSHA model
423 (Huang et al., 2015; Dong et al., 2016). In NACC-CMAQ, the potential for vertical dust flux in
424 FENGSHA is generally controlled by the sediment supply map (SSM), and the magnitude of the
425 friction velocity (USTAR) compared to a threshold friction velocity (UTHR) that determines the
426 USTAR needed to transfer dust from soil surfaces to the atmosphere. The UTHR is dependent on
427 the land cover and soil type, as well as the soil moisture. The SoilGrids™ 250-m high-resolution
428 dataset (<https://www.isric.org/explore/soilgrids>) provides the necessary clay, silt, and sand
429 fractions used to calculate the SSM. Tang et al. (2021b) further evaluates GBBEPx wildfire
430 smoke and FENGSHA windblown dust during air quality events predicted by NACC-CMAQ.

431 2.3 Updated Dynamic Aerosol Boundary Conditions

432
433 The chemical lateral boundary conditions (CLBCs) are critical to the prediction accuracy of
434 regional chemical transport models, particularly during intrusion events (Tang et al., 2009;
435 2021a). The CLBCs represent the spatiotemporal distribution of chemical species along the
436 lateral boundaries of the domain of a regional model. NACC-CMAQ uses methods described in
437 Tang et al. (2021a) and implements dynamic CLBCs (updated every 6-hours) for dust and smoke



438 aerosol data that are extracted (and mapped to CMAQ CB6-Aero7 species) from the NOAA
439 operational global atmospheric aerosol model, known as the Global Ensemble Forecast-Aerosols
440 (GEFS-Aerosols) member (Figure 2). GEFS-Aerosols is also based on the FV3GFS dynamical
441 core, which uses the Goddard Chemistry Aerosol Radiation and Transport (GOCART) model for
442 its sulfate, dust, BC, OC, and sea-salt aerosol predictions (Chin et al.; 2000; 2002; Ginoux et al.,
443 2001). GEFS-Aerosols uses the same wildfire smoke and windblown dust dataset/algorithms as
444 in NACC-CMAQ. The operational version of GEFS-Aerosols is run by the NWS as a special
445 unperturbed forecast of the Global Ensemble Forecast System version 12
446 ([https://www.ncdc.noaa.gov/data-access/model-data/model-datasets/global-ensemble-forecast-](https://www.ncdc.noaa.gov/data-access/model-data/model-datasets/global-ensemble-forecast-system-gefs)
447 [system-gefs](https://www.ncdc.noaa.gov/data-access/model-data/model-datasets/global-ensemble-forecast-system-gefs)), which provides an ensemble forecast product four times per day. Dynamic CLBCs
448 capture the signals of aerosol intrusion events such as biomass burning or windblown dust
449 plumes from outside the domain, which can improve the prediction accuracy of downstream O₃
450 and PM_{2.5} concentrations at the surface (Tang et al., 2021a).

451 3. Simulation Design and Evaluation Protocol

452
453 Table 1 summarizes the GFSv16/NACC-CMAQv5.3.1 model configuration described in
454 Section 2, as well as some additional model details. The model components and configurations
455 used in prior NAQFC system are summarized in Table S2 (based on Lee et al., 2017) for
456 comparison.

457

458

459

460



461 **Table 1. GFSv16/NACC-CMAQv5.3.1 model components and configurations.**

Model Attribute	Configuration	Reference
Domain	Contiguous U.S.; Center = 40°N;97°W	n/a
Horizontal Resolution	12 km	n/a
Vertical Resolution	35 Layers from near-surface to about 14 km (~ 60 hPa)	n/a
Meteorological ICs and BCs	FV3GFSv 16	https://nws.weather.gov/
Chemical ICs and BCs	2006 GEOS-Chem Simulation & GEFS-Aerosol Dynamic Smoke and Dust Aerosol CLBCs	http://acmg.seas.harvard.edu/geos/ <i>Tang et al. (2021a)</i>
Anthropogenic Emissions	NEIC 2016v1 Platform	<i>NEIC (2019)</i>
Biogenic Emissions	Inline BEISv3.6.1 & BELD5	<i>Vukovich and Pierce (2002); Schwede et al. (2005)</i>
Wildfire Emissions/Plume Rise	GBBEPxv3/ Inline Briggs	https://www.ospo.noaa.gov/Products/land/qbbepx <i>Briggs (1965)</i>
Microphysics	GFDL six-category cloud microphysics scheme	<i>Lin et al., 1983; Lord et al., 1984; Krueger et al., 1995; Chen and Lin, 2011; Chen and Lin, 2013</i>
PBL Physics Scheme	sa-TKE-EDMF	<i>Han and Bretherton (2019)</i>
Shallow/Deep Cumulus Parameterization	SAS Scheme	<i>Han et al. (2011; 2017)</i>
Shortwave and Longwave Radiation	RRTMg	<i>Mlawer et al. (1997); Clough et al. (2005); Iacono et al. (2008)</i>
Land Surface Model	Noah Land Surface Model	<i>Chen and Dudhia (2001), Ek et al. (2003), Tewari et al. (2004)</i>
Surface Layer	Monin-Obukhov	<i>Monin-Obukhov (1954); Grell et al. (1994); Jimenez et al. (2012)</i>
Gas-phase Chemistry	CB6	<i>Yarwood et al., 2010</i>
Aqueous-phase Chemistry	CMAQ AQChem Updates	<i>Martin and Good (1991); Alexander et al. (2009); Sarwar et al. (2011)</i>
Aerosol Module/Size	AERO7	<i>Appel et al. (2021)</i>
Other Model Attributes	-In-line Photolysis	<i>Binkowski et al. (2007)</i>



	-In-line Bi-Directional NH ₃ Exchange	<i>Nemitz et al., 2000; Cooter et al., 2010; Massad et al., 2010; Pleim and Ran, 2011; Bash et al., 2010, 2013; Pleim et al., 2013; 2019</i>
	-In-line FENGSHA Wind-Blown Dust Emissions	<i>Fu et al., 2014; Huang et al., 2015; Dong et al., 2016</i>
	-In-line Sea-salt Emissions	<i>Kelley et al. (2010)</i>

462

463 The simulation design consists of evaluations of one-month, continuous NACC-CMAQ
 464 (72-hr, 3-day forecast) and prior NAQFC (48-hr, 2-day forecast) simulations for September 2020
 465 (late summer/fall period) and January 2021 (winter period) (with previous 1-month spin-up and
 466 training-data period) over CONUS at a horizontal grid spacing of 12 km (Table 1). September
 467 2020 is used for the warm season because it is the closest month to summer when both the
 468 NACC-CMAQ and prior operational NAQFC systems were simultaneously run. The prior
 469 operational NAQFC was discontinued on July 20, 2021 due to computational constraints at
 470 NWS/NOAA.

471 The Surface Weather Observations and Reports for Aviation Routine Weather Reports
 472 (METAR), collected by NCEP's Meteorological Assimilation Data Ingest System (MADIS)
 473 (https://madis.ncep.noaa.gov/madis_metar.shtml), provide observations of TEMP2, 2-m specific
 474 humidity (Q2), and 10-m wind speed (WSPD10). The World Radiation Monitoring Center's
 475 (WRMC's) Baseline Solar Radiation Network (BSRN) ([https://](https://bsrn.awi.de/)
 476 bsrn.awi.de/; Driemel et al., 2018) and U.S. Surface Radiation Network (SURFRAD;
 477 <https://gml.noaa.gov/grad/surfrad/>) provide shortwave radiation observations at the ground
 478 (SWDOWN). The PRISM Climate Group, Northwest Alliance for Computational Science and
 479 Engineering, at Oregon State University (<https://prism.oregonstate.edu/>; Accessed on 05 May
 480 2021) provide gridded total precipitation observations (PRECIP). The National Oceanic and



481 Atmospheric Administration (NOAA), Earth System Research Laboratory's (ESRL's)
482 Radiosonde Database (RAOB) (<https://ruc.noaa.gov/raobs/>) provide vertical profile observations
483 of temperature, relative humidity, and wind speed. The U.S. EPA Air Quality System (AQS;
484 <https://www.epa.gov/aqs>) and near-real-time AirNow observational networks
485 (<https://www.airnow.gov/>) provide near-surface O₃ and PM_{2.5} measurements.

486 The statistical measures used to evaluate the meteorological-chemical/air quality
487 predictions include the mean bias (MB), normalized mean bias (NMB), normalized mean error
488 (NME), Root Mean Square Error (RSME), Anomaly Correlation Coefficient (ACC), Pearson's
489 correlation coefficient (R), and Index of Agreement (IOA). Statistical measures such as R, NMB,
490 and NME provide measures of the associativity (i.e., correlation), bias, and accuracy,
491 respectively, of specific modeled surface and vertical meteorology and surface O₃ and PM_{2.5}.
492 The meteorological and chemical evaluations use the publicly available U.S. EPA Atmospheric
493 Model Evaluation Tool (AMET; Appel et al., 2011) and NOAA/ARL Model and Observation
494 Evaluation Toolkit (MONET; Baker et al., 2017). A more detailed diagnostic evaluation for the
495 numerous science advancements (Figure 2) in NACC-CMAQ compared to the prior NAQFC, as
496 well as additional meteorological, trace gas, and PM_{2.5} composition comparisons is shown in
497 Tang et al. (2021b).

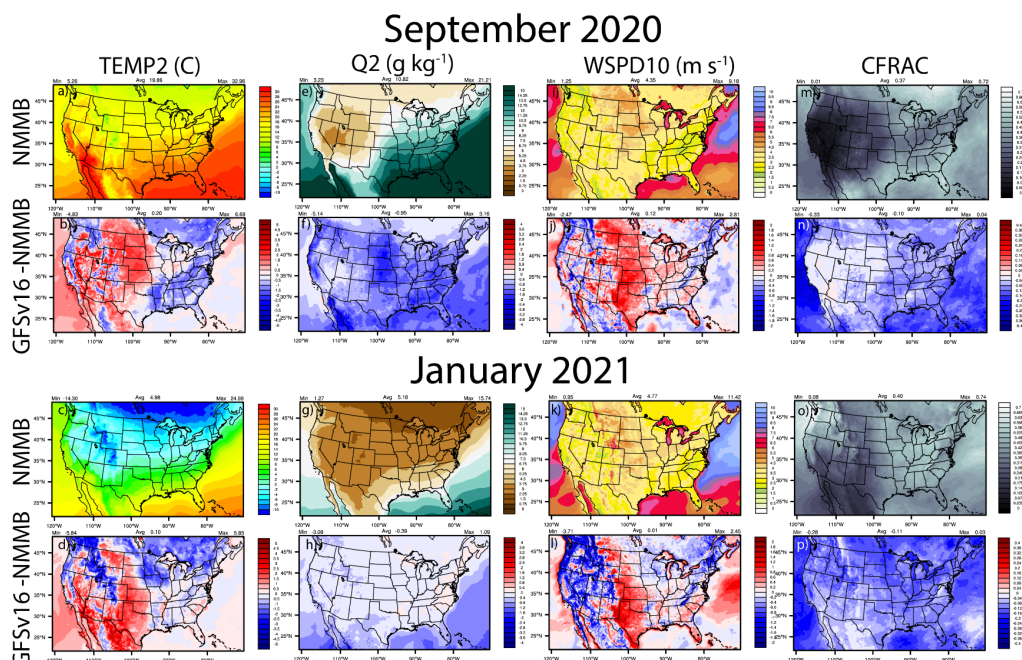
498 **4. Results**

499 500 4.1 Meteorological Analysis

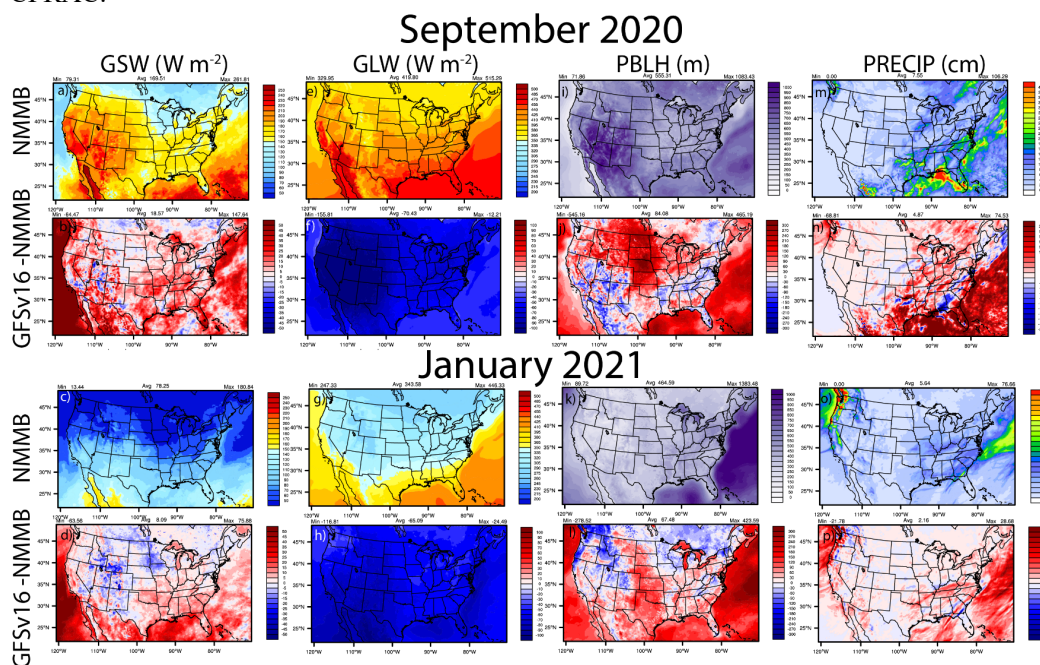
501 Compared to NMMB used in the prior NAQFC, the GFSv16 model has lower actual
502
503 TEMP2 in the east-southeast and parts of the northwest (Figures 4a-d), but has higher TEMP2 in
504 the central, northern plains, and parts of the west-southwest U.S. with higher 10-meter wind
505 speeds (WSPD10) in these regions (Figures 4i-l). GFSv16 is drier with widespread lower 2-



506 meter specific humidity (Q2; Figures 4e-h) and lower cloud fractions (CFRAC) (Figures 4m-p),
507 higher solar radiation absorbed at the ground (GSW; Figures 5a-d), lower longwave radiation
508 absorbed at the ground (GLW; Figures 5e-h), deeper planetary boundary layer height (PBLH;
509 Figures 5i-l), and generally more regions of increased precipitation (PRECIP; Figures 5m-p).
510 Differences in the CFRAC are (in part) impacted by differences in the model definition of cloud
511 cover; NMMB uses a binary cloud cover definition at each grid point, while GFSv16 uses
512 fractional cloud cover to calculate CFRAC. The PBLH in the prior NAQFC is re-diagnosed
513 based on the Troen and Mahrt (1986) incremental calculation of the bulk Richardson number
514 (Ri_b) from the surface up to a height above the neutral buoyancy level in the Asymmetric
515 Convective Model v2 (ACM2) PBL scheme in CMAQ (Pleim 2007a;2007b). NACC-CMAQ
516 directly uses the diagnosed PBLH from the Turbulent Kinetic Energy (TKE)-based PBL scheme
517 in GFSv16 (Table 1; Han and Bretherton, 2019), which is also based on the Troen and Mahrt
518 (1986) Ri_b methodology with slight differences in some internal parameters (e.g., critical
519 Richardson number) compared to ACM2.



522 **Figure 4.** September 2020 and January 2021 spatial average plots for NMMB (prior NAQFC)
 523 and the absolute differences for GFSv16 (NACC) - NMMB for TEMP2, Q2, WSPD10 and
 524 CFRAC.



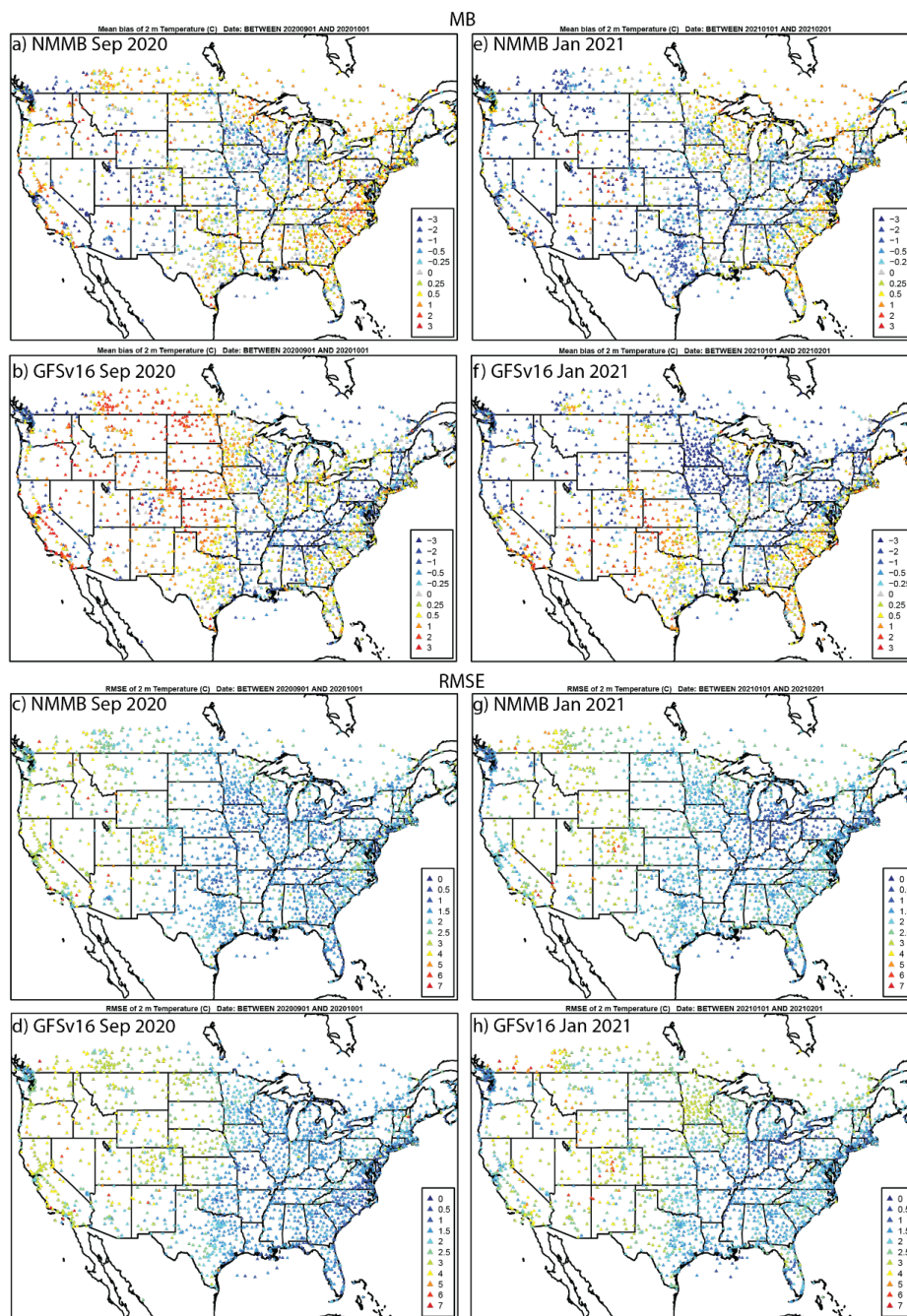
526 **Figure 5.** Same as in Figure 4 but for GSW, GLW, PBLH, and PRECIP.



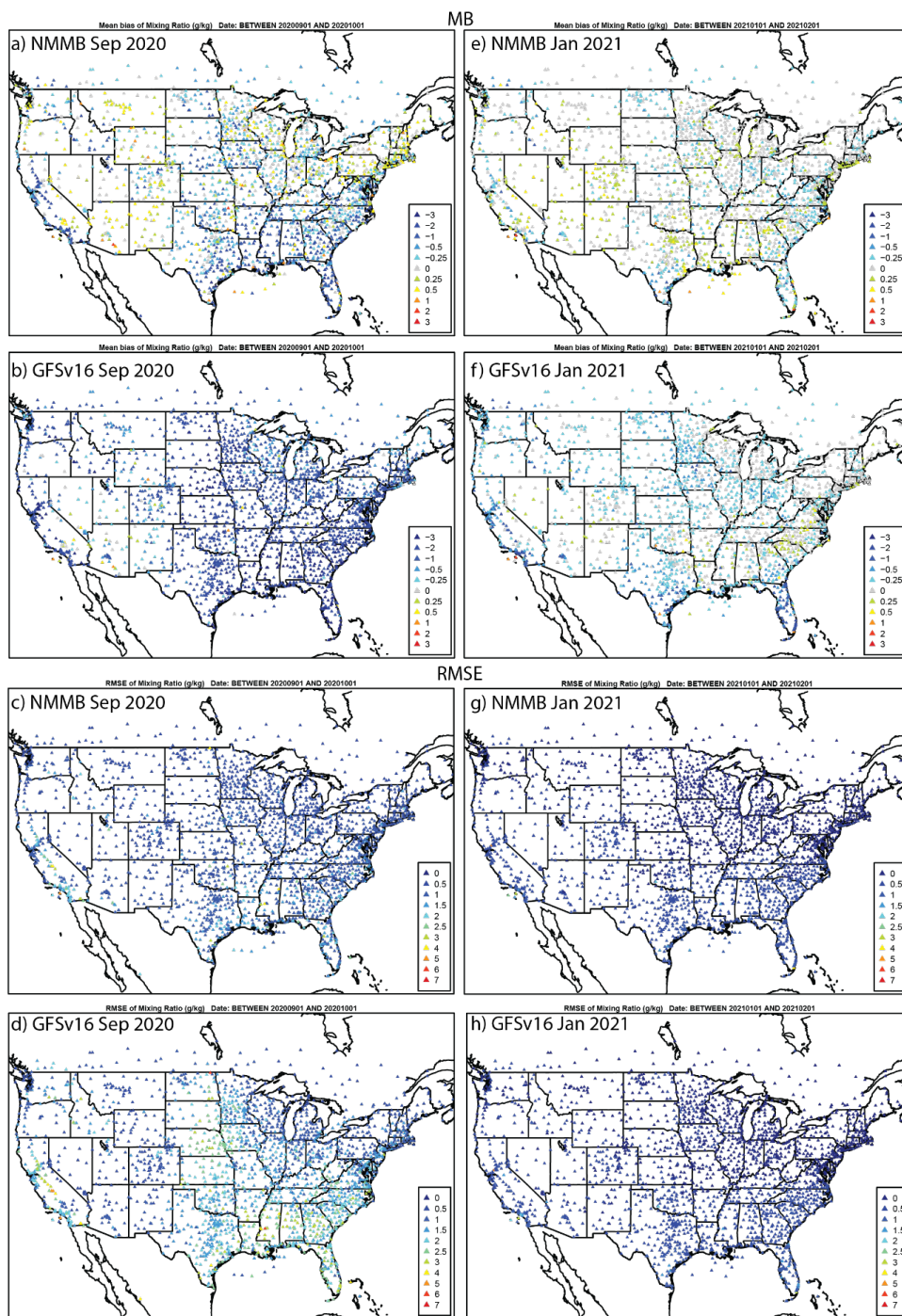
527 The GFSv16 (NACC) and re-diagnosed ACM2 (prior NAQFC) diurnal PBLH patterns are
528 similar at night; however, the GFSv16 PBLH is considerably higher than NAQFC during the
529 daytime for all regions in September and January (Supporting Figures S4-S5).

530 The meteorological differences between GFSv16 and NMMB (Figures 4-5) influence
531 chemical predictions in CMAQ, which include a deeper daytime PBL and more precipitation that
532 can effectively dilute the gaseous and aerosol concentrations for NACC-CMAQ in some regions
533 across CONUS. Areas of lower CFRAC and higher TEMP2 and GSW in GFSv16, however,
534 will increase photolysis and daytime O₃ formation in NACC-CMAQ in certain regions including
535 the south and upper Great Plains U.S. Considering the PBLH calculation methodologies are
536 similar between the prior NAQFC and NACC-CMAQ (based on Troen and Mahrt (1986) with
537 differences in some internal parameters), the differences in near-surface meteorology (i.e.,
538 generally warmer/drier) conditions in the GFSv16 (Table 2 and Table S2) are driving the
539 differences in PBLH (Figures 5i-l). These differences affect the pollutant mixing and dilution,
540 and in part, the resulting air quality predictions between the prior NAQFC and NACC-CMAQ
541 (see Section 4.3 below).

542 Evaluation of the simulated day 1 (0-24 hr) forecasted meteorology against the METAR
543 network shows that GFSv16 generally has a higher positive TEMP2 (warmer) bias (Figure 6) in
544 the west, and has a CONUS-wide higher negative Q2 (dry) bias (Figure 7) compared to prior
545 NMMB (i.e., prior NAQFC) in both September and January.



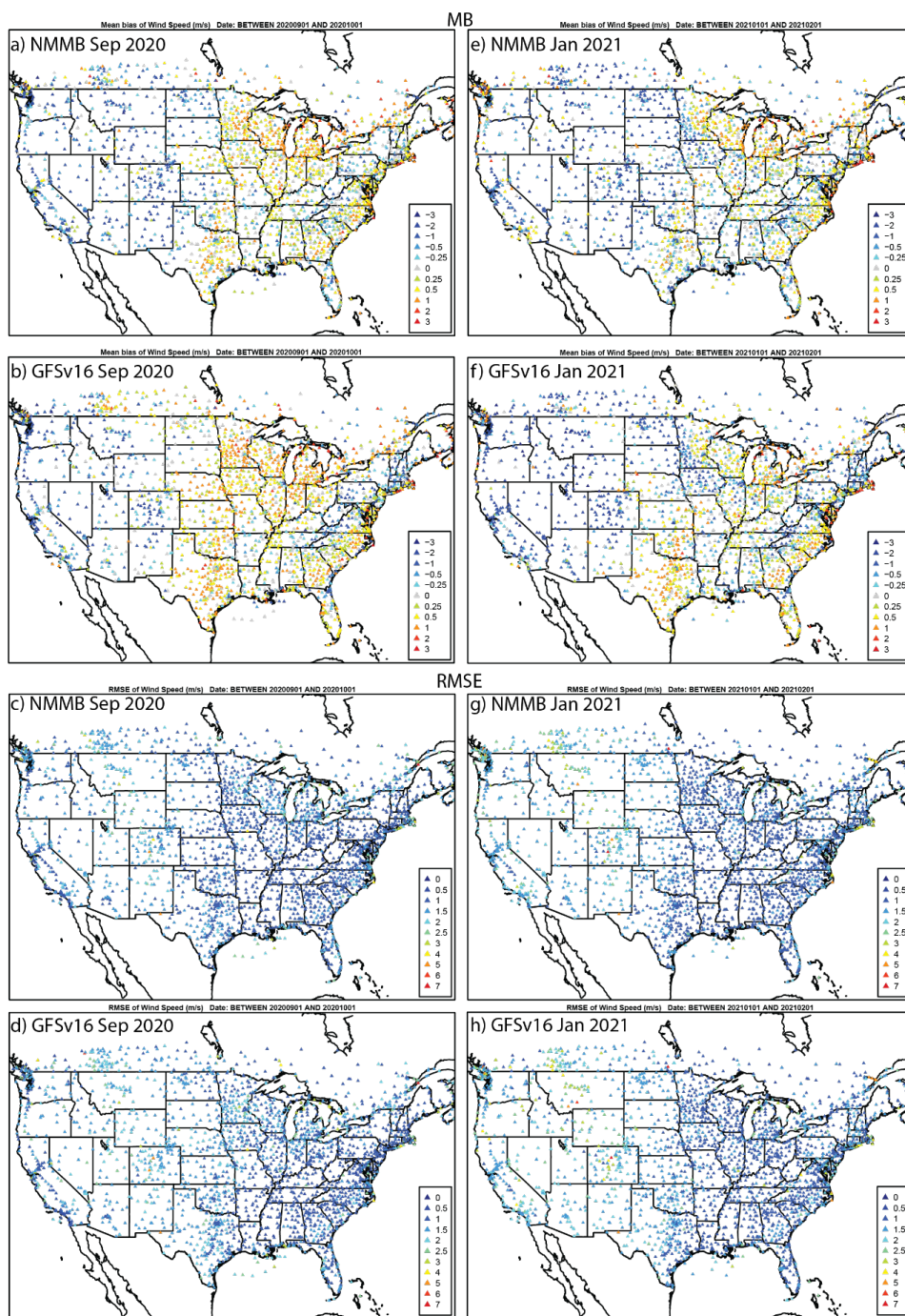
547 **Figure 6.** Average day 1 (0–24 hr) forecasted TEMP2 MB (°C) and RMSE (°C) for NMMB and
548 GFSv16 during a)–d) September 2020 and e)–h) January 2021 compared to METAR
549 observations.



551 **Figure 7.** Same as in Figure 6, but for Q2 (g kg^{-1}).



552 There are regions of higher RMSE for T2 and Q2, and lower/degraded ACC (Figures S7-S8) for
553 GFSv16 compared to NMMB, especially in the southern and western CONUS regions during
554 September. The spatial patterns and magnitudes of WSPD10 bias and error are similar between
555 GFSv16 and NMMB (Figure 8); however, the higher WSPD10 for GFSv16 in the southern and
556 central CONUS leads to a shift from negative to positive biases from Texas northward to North
557 Dakota, especially during September. The WSPD10 RMSE is higher (Figure 8) and the ACC is
558 also lower/degraded (Figure S9) for GFSv16 in those regions, otherwise, the GFSv16 and
559 NMMB have similar performance for WSPD10. The day 1 forecast model performance (MB,
560 RMSE, and ACC) for 10-m wind direction (WDIR10) is similar between NMMB and GFSv16 in
561 both September and January (Figs. S6 and S10).



563 **Figure 8.** Same as in Figure 6, but for WSPD10 (m s^{-1}).



564 Overall, the GFSv16 results are favorable for driving the advanced NACC-CMAQ
565 system, with some areas of concern in the degraded TEMP2 and Q2 in the warmer/drier regions,
566 particularly in the south and west CONUS during September. This roughly correlates with
567 warmer/drier top-layer soil conditions in GFSv16 in these regions (Fig. S11), and thus land
568 surface/soil data assimilation and model development and improvement in GFSv16 is an active
569 area of focus at NOAA. The widespread dry bias in GFSv16 appears to be persistent, as an
570 independent evaluation of August 2019 demonstrated very similar spatial patterns and magnitude
571 of Q2 underpredictions in the eastern half of CONUS compared to the METAR network (not
572 shown).

573 The GFSv16-driven NACC-CMAQ system extends out to a 72-hour forecast. Hence,
574 there is a question of how the day 1 and 2 forecasts perform for NMMB vs. GFSv16 in the
575 eastern ($<100^\circ$ W) and western ($>100^\circ$ W) U.S., and how a day 3 forecast extension also affects
576 the GFSv16 diurnal and statistical model performance. The GFSv16/NACC diurnal patterns of
577 standard deviation, error, and bias for TEMP2, Q2, and WSPD10 are very similar to each other
578 for days 1-3 (Figures S12-14). While there is a slight increase in error and decreased correlation
579 (R), the relevant statistical metrics (e.g., MB, NMB, RMSE, and R) do not change appreciably
580 from day 1 to 3 for both September and January (Tables S3-S4). This lends confidence in the
581 utility of using the updated GFSv16 meteorology to drive a 72-hour air quality forecast in
582 NACC-CMAQ.

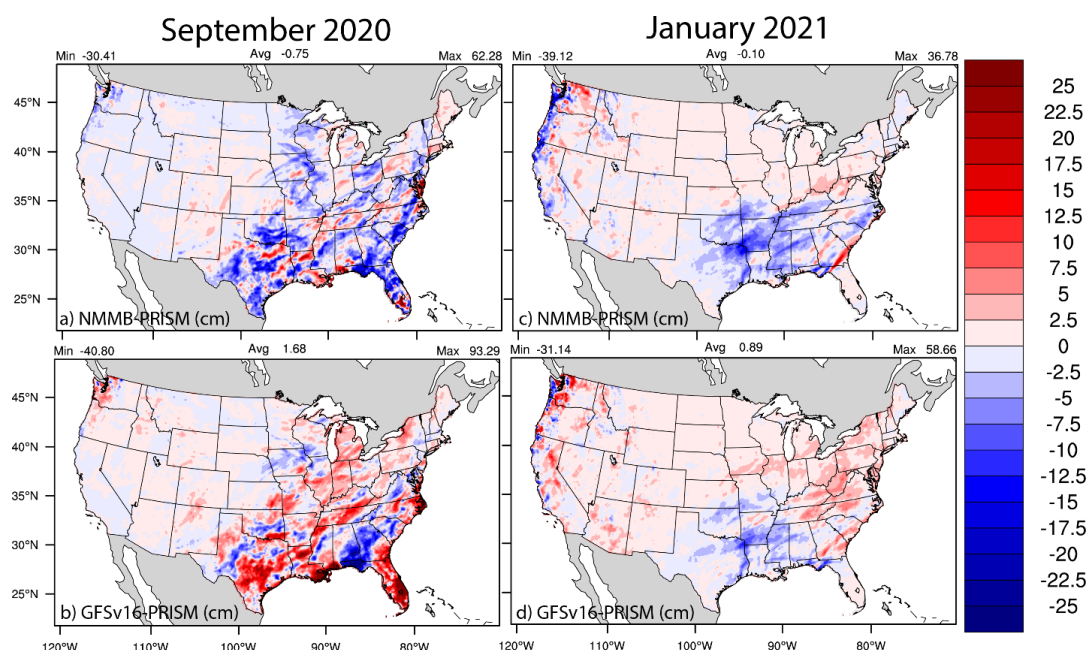
583 The day 1 diurnal statistics highlight both similar and contrasting TEMP2 and Q2
584 patterns for NMMB vs. GFSv16 in the eastern and western CONUS (Figures S12-S13). In
585 September (Figure S12a), NMMB has higher error and positive TEMP2 (i.e., warm) bias in
586 eastern CONUS during morning hours, and lower error with a slight cool bias in the



587 afternoon/evening, while GFSv16 shows slight overpredicted TEMP2 during most hours of the
588 day in the east. Over western CONUS, there are larger diurnal TEMP2 differences that include
589 small oscillating TEMP2 biases (about zero) for NMMB, along with distinctly large warm biases
590 during all daytime hours for GFSv16 in the west. There are larger error and negative Q2 (i.e.,
591 drier) biases for GFSv16 compared to NMMB in eastern and western CONUS (Figure S13a).
592 In January, the TEMP2 and Q2 diurnal statistical patterns are similar for NMMB and GFSv16 in
593 both the eastern and western CONUS; however, the GFSv16 daytime hours have slightly higher
594 error and warmer and drier biases compared to NMMB (Figures S12b and S13b).

595 The total PRECIP is generally higher in GFSv16 compared to NMMB out East (Figure
596 5), which leads to larger overpredictions on average in CONUS compared to PRISM (Figure 9).
597 GFSv16 has a positive PRECIP bias on average in CONUS, NMMB has a negative bias, and
598 there is relatively more difference in the spatial patterns between NMMB and GFSv16 for
599 September compared to January. The difference is impacted by higher convective activity
600 during late summer/early fall in September compared to winter in January (not shown). Further
601 analysis indicated that generally heavier PRECIP reduces the predicted PM_{2.5} concentrations via
602 wet deposition (not shown) in the east-southeast, and in parts of the west-northwest compared to
603 NMMB.

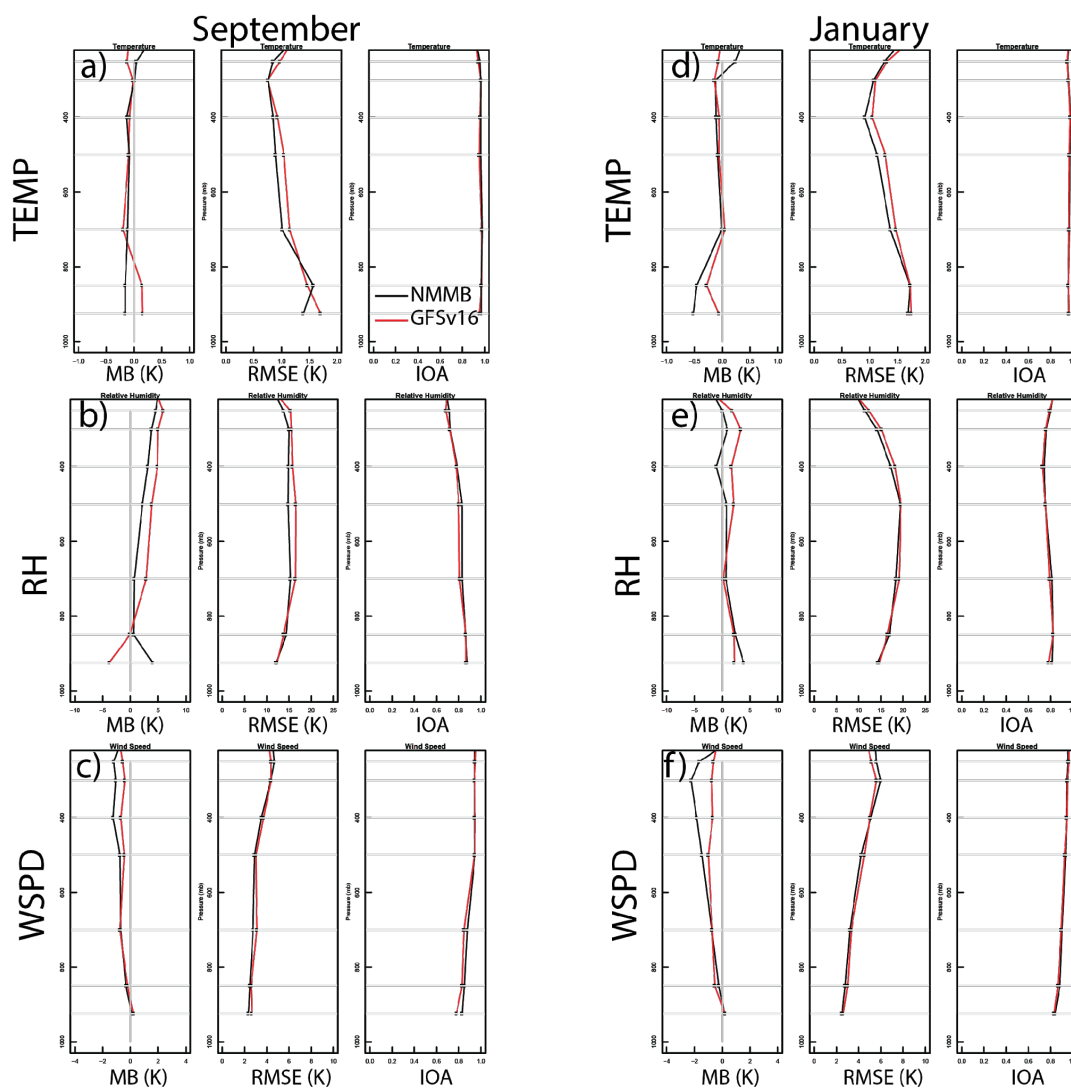
604



606 **Figure 9.** Average day 1 (0-24 hr) forecasted total PRECIP (cm) biases (Predicted-PRISM) for
607 NMMB (top) and GFSv16 (bottom) during a)-b) September 2020 and c)-d) January 2021.

608
609

Comparisons of the model vertical profile statistics (i.e., MB, RMSE, and IOA) for
610 TEMP, RH, and WSPD against an average of select RAOB observations across CONUS indicate
611 that the GFSv16 (NACC) performs consistently with the operational NMMB (NAQFC) column
612 (Figure 10; IOA nearly identical at ~0.8-0.9). GFSv16 is warmer and drier than NMMB in the
613 model layers near the surface (> 850 mb), especially in September; however, GFSv16 has a
614 moister atmospheric column with higher wind speeds compared to NMMB above the surface and
615 in the free troposphere (< 850 mb). Figures S15-S17 show the spatial variability across the
616 different RAOB sites used in the average for Figure 10. Analysis of the column (1000-250 hPa)
617 average for all CONUS RAOB sites across CONUS indicate that GFSv16 has a predominantly
618 cooler and moisture atmospheric column in September, despite being strongly warmer and drier
619 near the surface (Figures S18-S19).



621 **Figure 10.** September 2020 (left) and January 2021 (right) vertical (1000 – 250 mb) wind speed
622 (WSPD) statistics (MB, RMSE, and IOA) for NMMB (black) and GFSv16 (red) against an
623 average for select RAOB sites in CONUS. Supporting Figure S15a shows specific RAOB sites,
624 and Supporting Figures S18-S19 provides their relative locations.

625

626 4.2 Emissions Analysis

627

628 The updated NEIC2016v1 emissions in NACC-CMAQ are lower compared to the

629 NEI2014v2 emissions used in the operational NAQFC for all major species, except for NH₃



630 (Table 2), as the NEIC2016v1 includes updated data sources and model projections that
 631 projected decreasing emissions compared to the NEI2014v2 (NEIC, 2019).

632 **Table 2.** September and January emissions totals (Tg) for the NAQFC CONUS domain.

Emission Species	NEI2014v2	NEIC2016v1	% Difference
September Total (Tg)			
CO	4.69	4.27	-8.9
NO _x	0.92	0.75	-18.1
SO ₂	0.54	0.37	-31.2
NH ₃	0.48	0.59	23.9
AVOC	215.58	195.60	-9.3
POC	0.07	0.05	-26.8
PEC	0.03	0.02	-23.9
PMC	2.03	0.82	-59.3
January Total (Tg)			
CO	3.70	3.28	-11.2
NO _x	0.78	0.64	-18.5
SO ₂	0.58	0.38	-34.7
NH ₃	0.10	0.12	18.4
AVOC	182.02	174.05	-4.4
POC	0.08	0.07	-10.8
PEC	0.02	0.02	-16.7
PMC	1.27	0.24	-80.8

633 Red (blue) shading indicates total emissions increases (decreases).

634

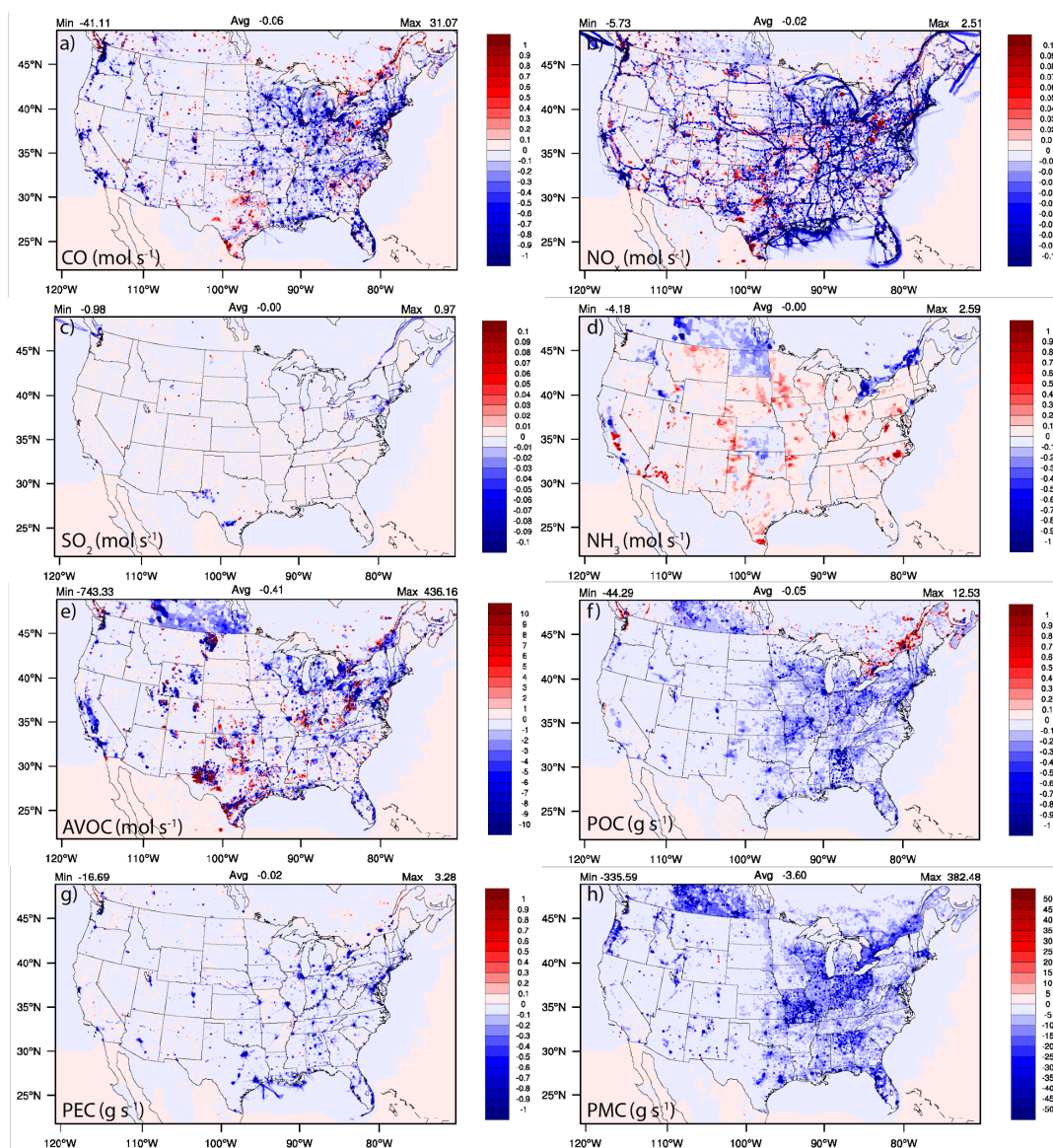
635

The spatial emission changes show widespread decreases in the 2D area/mobile

636 emissions near the major urban cities for CO and NO_x and across the major interstates and

637 railways for NO_x (Figures 11a-b).

638



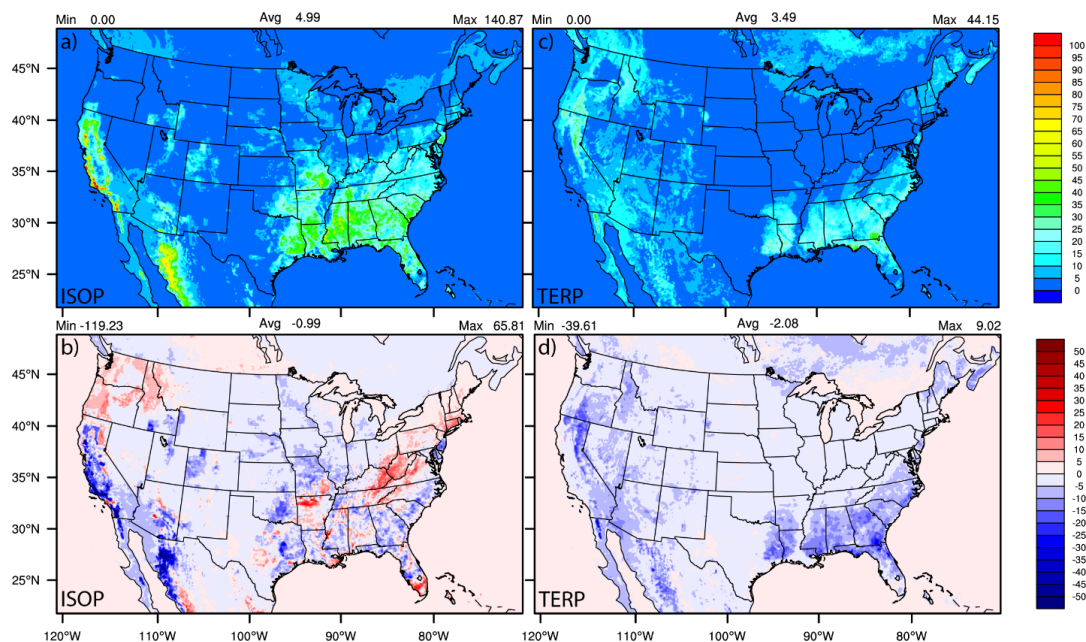
640 **Figure 11.** September 2020 average spatial difference plots for NEIC2016v1-NEI2014v2
641 combined 2D area/mobile emissions. Figure S20 shows very similar emission changes as
642 September, but for January 2021.

643
644 The spatial variability in NO_x emission changes, however, are impacted by changes in a number
645 of onroad inputs including vehicles miles traveled, age distribution, and speeds, which caused
646 some emissions to go up or go down depending on the specific counties. The NO_x emissions



647 variability is also impacted by national increases in railway levels and fuel use, while at the same
648 time being impacted by changes to fuel efficiency and cleaner engines for both passenger and
649 commuter trains. There are relatively minor area/mobile changes in SO₂ (Figure 11c), with some
650 exceptions in the east-northeast; however, there are widespread increases in NH₃ emissions
651 driven by changes to the livestock counts and updated fertilization methods and inputs found in
652 the NEIC2016v1 (Figure 11d). Changes in nonpoint oil and gas production, exploration, and
653 emission factors generation, as well as changes to updated activity and data sources for
654 commercial cooking, residential fuel combustion, and industrial/commercial/institutional (ICI)
655 fuel combustion impact the AVOC area emission changes (Figure 11e). The widespread, and
656 spatially consistent decreases in POC and PMC are due to decreasing fugitive dust sources
657 (Figures 11f and 11h); with the exception of the St. Lawrence River Valley, that has both
658 increases in POC and AVOC (e.g., formaldehyde; not shown) emissions in the NEIC2016v1.
659 Updated appliance counts and residential wood combustion estimates affect the PEC area
660 emission decreases (Figure 11g).

661 There are also biogenic emissions differences due to the updated inline BEISv3.6.1 and
662 BELD5 in NACC-CMAQ (Table 2), and due to the impacts of NMMB (prior NAQFC) vs.
663 GFSv16 (NACC) meteorology on BEIS calculations (Figure 12).



665 **Figure 12.** September 2020 average isoprene (ISOP) and terpene (TERP) emissions (top) in the
666 prior NAQFC with BEISv3.1.4, and the absolute differences (bottom) for NACC-CMAQ (with
667 BEISv3.6.1) - NAQFC.

668
669 The lower GFSv16 temperatures near many of the highly vegetated regions of the CONUS in
670 September (Figure 4b) decrease the isoprene (ISOP) and terpene (TERP) emissions, with some
671 notable, localized ISOP emission increases due to larger relative increases in downward solar
672 radiation at the surface (GSW; Figure 5b) and resulting Photosynthetic Active Radiation (PAR;
673 not shown). The differences are also impacted by the derivations of leaf temperatures in the
674 updated BEISv3.6.1 and BELD5 in NACC-CMAQ compared to the BEISv3.14 and BELD3 in
675 the prior NAQFC (see discussion in Section 2.2). Hence, the differences in spatial variability
676 between ISOP and TERP emission changes stem from both differences in the locations of their
677 relative maxima, and from the different algorithms for temperature and light dependencies in
678 BEIS. The GFSv16 (NACC) performs very similarly to NMMB (prior NAQFC) for GSW at the
679 surface compared against BSRN-SURFRAD observations in CONUS, with a slightly larger



680 overprediction in the late afternoon at some sites (Figures S21 and S22). The relatively lower
681 ISOP and TERP emissions in NACC-CMAQ will effectively lower the ground-level O₃ and
682 contribution of secondary organic aerosol (SOA) formation to PM_{2.5} compared to the prior
683 NAQFC, particularly in the southeast and parts of the western CONUS in the late summer/early
684 fall. This is somewhat mitigated by enhanced GSW in NACC-CMAQ.

685 4.3 Air Quality Analysis

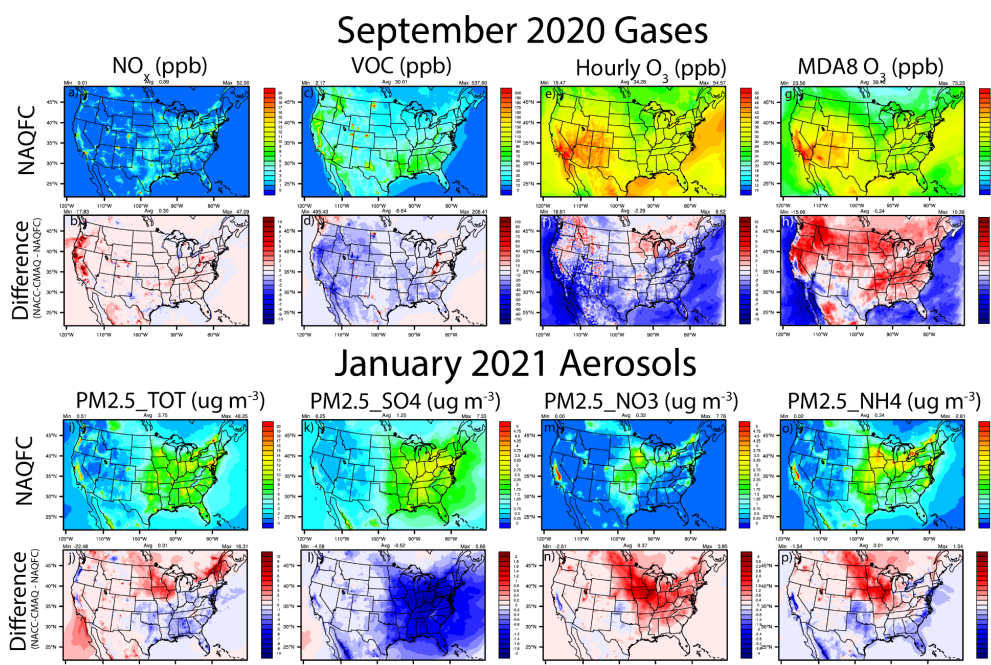
686

687 Here we focus on analysis of NACC-CMAQ predictions of gaseous O₃ for the late
688 summer/early fall (September 2020) and PM_{2.5} concentrations during the winter (January 2021)
689 as concentrations are relatively higher for the pollutant's respective seasons. Analysis of NACC-
690 CMAQ gaseous and particulate matter predictions are expanded to other months/seasons in Tang
691 et al. (2021b). During the late U.S. ozone season in September 2020, a large majority of the
692 local NO_x concentration increases in NACC-CMAQ (Figures 13a-b) correlate with areas of NO_x
693 emissions increases in the NEIC2016v1 compared to the NEI2014v2 (Figure 11b). An exception
694 is the large NO_x increases in the far west (e.g., California and Oregon) that stem from gaseous
695 NO_x emissions from strong wildfires that are captured by the GBBEPx in NACC-CMAQ (Table
696 1) but are excluded from the prior NAQFC wildfire emissions system (Table S2). Analyses of
697 the gaseous NO_x emissions effects in NACC-CMAQ is further explored in Tang et al. (2021b).

698

699

700



701

705 The increases in NO_x concentrations and enhanced nighttime O₃ titration, widespread decreases
706 in total VOC concentrations due to both anthropogenic and biogenic VOC emission decreases in
707 NACC-CMAQ, and GFSv16-meteorology effects (e.g., higher PBLH) lead to widespread
708 decreases in hourly O₃ when averaged over all hours (Figures 13e-f). Regions of higher NO_x
709 emissions, overall drier (i.e., widespread lower Q2) conditions, and stronger mid- to late-
710 afternoon solar radiation at the surface (i.e., widespread higher GSW) (see Figures 4-5 and
711 Figures S21-22) lead to enhanced daytime O₃ formation, which is shown in the widespread
712 increases in the maximum daily 8-hr average (MDA8) O₃ for NACC-CMAQ (Figures 13g-h).
713 This is particularly true for the strong NO_x-limited conditions in the western CONUS, where the
714 MDA8 O₃ increases are impacted by large increases in wildfire NO_x emissions in GBBEPx and
715 VOC decreases (anthropogenic+biogenic, but no wildfire VOC emission impacts) in NACC-
716 CMAQ. These effects subsequently impact the ozone NO_x-VOC sensitivity/regime that



717 enhances the NO_x-saturated (i.e., VOC-limited) conditions in this case (Figure S24). There are
718 exceptions with MDA8 O₃ decreases in the west, including western Oregon, the San Joaquin
719 Valley in California, and regions of the southwest CONUS, all of which are strongly VOC-
720 limited (Figure S24). These regions are further impacted by the VOC decreases and further NO_x
721 saturation from wildfire emissions in some locations of the west. Further details on the CONUS
722 August-September 2019-2020 wildfire emissions impacts on both O₃ and PM_{2.5} in the prior
723 NAQFC compared to NACC-CMAQ are provided in Tang et al. (2021b). The widespread
724 decreases in both the hourly and MDA8 O₃ over all oceanic regions in the domain are driven by
725 the updated halogen (e.g., bromine and iodine chemistry) mediated O₃ loss in NACC-CMAQ,
726 which can reduce annual mean surface ozone over seawater by 25% (Sarwar et al., 2019).

727 There are both relatively large increases (north, northeast and west) and decreases (south-
728 southeast and parts of the west) for winter (January 2021) total PM_{2.5} (PM25_TOT) in CONUS
729 for NACC-CMAQ compared to NAQFC (Figures 13i-j). The decreases in inorganic
730 PM25_TOT in the east-southeast are dominated by decreases in particulate sulfate (PM25_SO4)
731 and ammonium (PM25_NH4), while the increases in the north-central eastern CONUS are
732 driven by increases in particulate nitrate (PM25_NO3) and PM25_NH4. Further analysis
733 indicates that the widespread decreases in PM25_SO4, most prolifically in the east, are driven
734 strongly by widespread lower CFRAC in GFSv16 (Figure 4o-p) and lower aqueous-phase
735 oxidation in CMAQ (not shown). There are also contributions from decreased SO₂ emissions
736 found in some CONUS regions for NACC-CMAQ (e.g., northeast; Figure 11c). Additional
737 consumption of inorganic sulfate as secondary isoprene epoxydiol (IEPOX) organosulfates are
738 formed in the updated AERO7 aerosol mechanism in NACC-CMAQ (Table 1; Pye et al. 2013,



739 2017), and further contribute to the PM25_SO4 decreases. The higher total PRECIP for NACC-
740 CMAQ (Figure 5) also leads to lower PM25_TOT in the east-southeast regions.

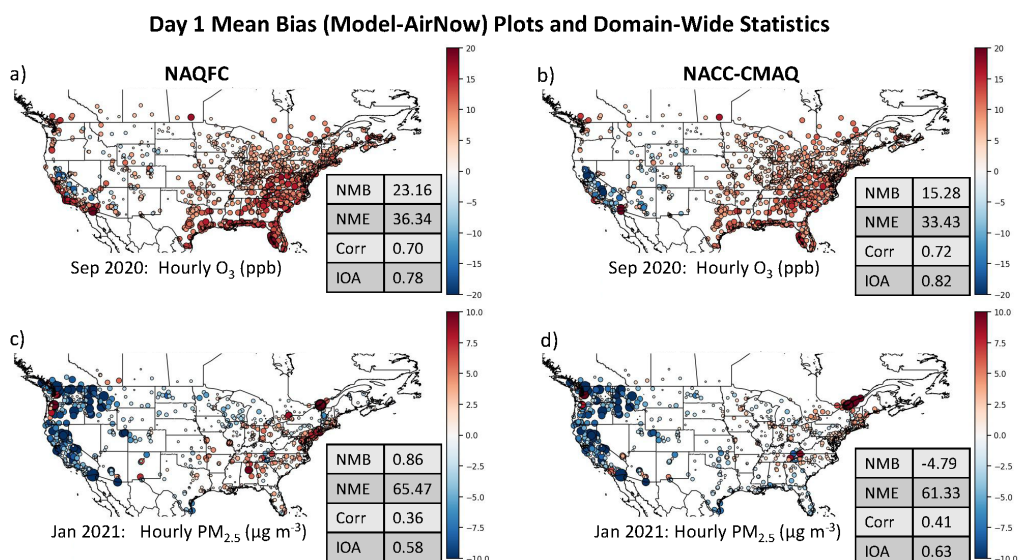
741 The largest PM25_TOT increases in the north-central CONUS are primarily driven by
742 enhanced ammonium nitrate formation, PM25_NO3 and PM25_NH4, which are influenced by
743 increases in NH3 emissions (Figure 11) and the inclusion of BIDI-NH3 fluxes in NACC-CMAQ
744 (Table 1). BIDI-NH3 in NACC-CMAQ allows for inline calculation of the diurnal pattern of
745 both NH3 evasion/emission and deposition, while the prior NAQFC only includes deposition.
746 Consequently, BIDI-NH3 in NACC-CMAQ generally increases ambient NH4⁺ and NO3⁻ aerosol
747 concentrations (Bash et al., 2013; Pleim et al., 2019) compared to the prior NAQFC.

748 There are also contributions to the increased PM25_TOT from organic carbon sources
749 (Figure S25; PM25_OC), especially in the northeastern portion of the domain that include the St.
750 Lawrence River Valley region. This is in part due to enhanced anthropogenic VOC emissions in
751 NEIC2016v1 (Figure 11e, e.g., formaldehyde; not shown) and more aggressive AERO7
752 secondary organic aerosol formation in this region for NACC-CMAQ (not shown). There are
753 also small PM25_EC contributions to the PM25_TOT decreases in the east and increases in the
754 west for NACC-CMAQ (Figure S25), which are mainly due to decreases in anthropogenic PEC
755 emissions in the east (Figure 11g), but also from contributions of relatively small GBBEPx
756 wildfire PM emissions in the west (not shown). The prior NAQFC does not include wildfire
757 smoke emissions during the month of January.

758 Evaluation of NACC-CMAQ shows overall improvement in the spatial MB of hourly O3
759 (September) and PM2.5 (January) against the AirNow network across CONUS (Figure 14).
760 There are clear reductions in the NAQFC overpredictions of O3 and PM2.5 in the east, and overall
761 reduction in NME, and overall improved correlation (R) and IOA for NACC-CMAQ. There are



762 also reduced overpredictions in the west for O₃ in September. The shifts to lower concentrations
763 result in larger domain-wide average PM_{2.5} underpredictions for NACC-CMAQ compared to the
764 prior NAQFC (cf. Figure 13 above); however, *the improvements in R and IOA for NACC-*
765 *CMAQ are substantial.* The MDA8 O₃ spatial MB evaluation against AirNow behaves similarly
766 to NAQFC, with slight degradation in the model performance statistics because of areas of
767 higher overpredictions in the eastern U.S due to reasons discussed above for enhanced daytime
768 O₃ formation in NACC-CMAQ (Figure S26).



769

774

775

776

777

778

The Day 2 forecasts have similar spatial model performance and statistics, with improved hourly O₃ and PM_{2.5} model performance (Figure S27) and slightly higher MDA8 O₃ overpredictions in the east for NACC-CMAQ (Figure S28). The consistent model performance

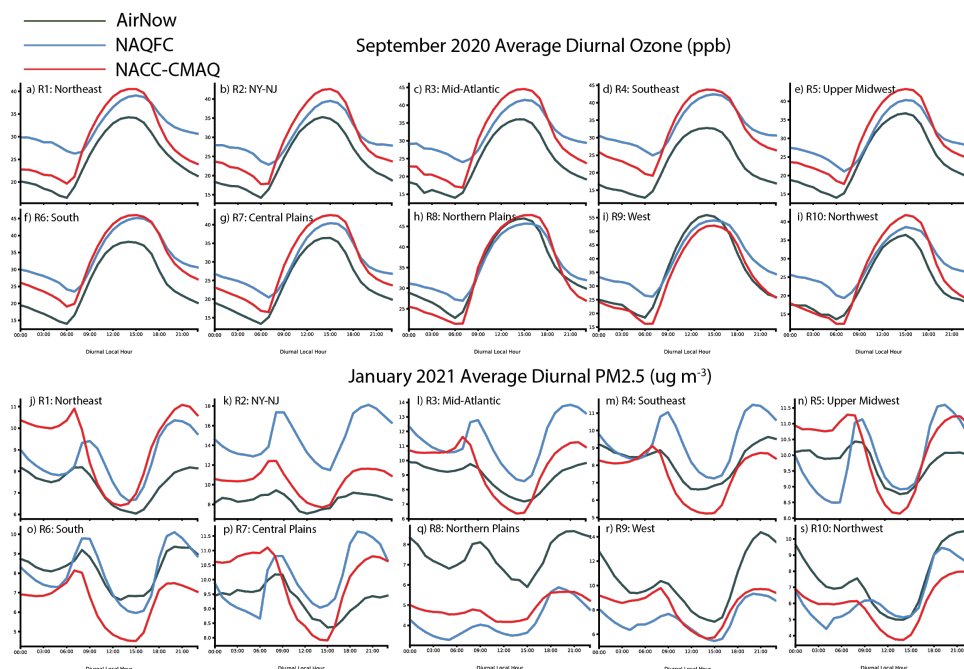


779 for Day 3 also shows utility in extending to 72-hr air quality forecasts in the advanced NACC-
780 CMAQ system (Figures S29-30). There is, however, a more notable degradation in skill for the
781 Day 3 forecast of PM_{2.5} compared to O₃ in NACC-CMAQ (compare Figures 14 and S29).

782 There is significant improvement in the average O₃ and PM_{2.5} diurnal patterns for each
783 CONUS region, other than higher daytime O₃ peaks for NACC-CMAQ compared to prior
784 NAQFC (Figure 15a-i). This is reflected in the improved R and IOA over CONUS on average
785 for NACC-CMAQ (Figure 14a-b). There is improved day-to-night O₃ transition, i.e., a sharper
786 slope or cutoff of daytime O₃ formation, which leads to lower nighttime O₃ mixing ratios in
787 NACC-CMAQ that agree better with AirNow observations for all CONUS regions.

788 The NACC-CMAQ PM_{2.5} diurnal pattern also is more consistent with AirNow for most
789 CONUS regions (Figure 15j-s), which is supported by improved R and IOA (Figures 14c-d).
790 There are, however, some regions (e.g., northeast, south, and northwest) that the prior NAQFC
791 shows better diurnal performance in this case.

792



793
794 **Figure 15.** Average September 2020 O₃ (top) and January 2021 PM_{2.5} (bottom) diurnal patterns
795 for NAQFC (blue), NACC-CMAQ (red), and AirNow observations (green) for different regions
796 in CONUS. The regions are based on [https://www.epa.gov/aboutepa/regional-and-geographic-](https://www.epa.gov/aboutepa/regional-and-geographic-offices)
797 [offices](https://www.epa.gov/aboutepa/regional-and-geographic-offices).

806
807
808
809
810
811



812 **Table 3.** Average September 2020 hourly O₃ evaluation of the operational NAQFC and NACC-CMAQ
 813 Day 1 forecasts against the AirNow network in different CONUS regions (based on
 814 <https://www.epa.gov/aboutepa/regional-and-geographic-offices>). Statistical benchmark values based on
 815 Emery et al. (2017) are also shown for comparison. Following Emery et al., a >40 ppb (i.e., daytime)
 816 cutoff for hourly O₃ is applied for the mean observations, mean models, mean bias, and the calculated
 817 values of NMB and NME, but not for the correlation value (r) or index of agreement (IOA). Total # of
 818 obs-model pairs are based on all values (i.e., no cutoff). **Blue** (**red**) shading indicates **improved** (**degraded**) NACC-CMAQ performance.
 819 Emery et al. criteria. **Blue** (**red**) shading indicates **improved** (**degraded**) NACC-CMAQ performance.
 820 Supporting Tables S5-S10 provide Day 2 and Day 3 (NACC-CMAQ only) forecast evaluations.

Day 1 Forecasts	Total # of Pairs	Mean Obs (ppb)	Mean Mod (ppb)	Mean Bias (ppb)	NMB (%)	NME (%)	Corr (r)	IOA
Benchmark Emery et al. (2017)	-	-	-	-	Goal: <±5% Criteria: <±15%	Goal: <15% Criteria: <25%	Goal: >0.75 Criteria: >0.50	-
Region 1 (Northeast)								
NAQFC	35983	46.85	43.55	-3.31	-7.06	15.04	0.61	0.71
NACC-CMAQ			43.44	-3.42	-7.29	15.14	0.70	0.81
Region 2 (NY-NJ)								
NAQFC	22944	46.68	42.90	-3.77	-8.09	17.88	0.59	0.72
NACC-CMAQ			45.18	-1.50	-3.21	14.27	0.72	0.81
Region 3 (Mid-Atlantic)								
NAQFC	89069	46.66	44.29	-2.37	-5.09	12.84	0.65	0.73
NACC-CMAQ			45.81	-0.85	-1.83	13.48	0.74	0.82
Region 4 (Southeast)								
NAQFC	105858	44.62	45.93	1.31	2.93	13.37	0.61	0.65
NACC-CMAQ			47.99	3.37	7.55	14.91	0.74	0.75
Region 5 (Upper Midwest)								
NAQFC	109744	46.61	43.84	-2.77	-5.94	13.28	0.69	0.77
NACC-CMAQ			46.59	-0.03	-0.05	10.69	0.77	0.83



Region 6 (South)								
NAQFC	84005	48.17	47.18	-0.99	-2.06	13.17	0.68	0.75
NACC-CMAQ			47.81	-0.36	-0.75	12.80	0.75	0.81
Region 7 (Central Plains)								
NAQFC	27139	44.98	44.84	-0.14	-0.31	10.45	0.76	0.81
NACC-CMAQ			47.18	2.20	4.90	9.54	0.82	0.86
Region 8 (Northern Plains)								
NAQFC	51759	48.97	44.64	-4.32	-8.83	13.89	0.71	0.82
NACC-CMAQ			45.08	-3.89	-7.95	14.00	0.72	0.85
Region 9 (West)								
NAQFC	124051	55.44	50.29	-5.15	-9.29	18.37	0.69	0.79
NACC-CMAQ			46.37	-9.07	-16.37	21.78	0.71	0.83
Region 10 (Northwest)								
NAQFC	14139	48.41	39.37	-9.03	-18.66	21.59	0.61	0.72
NACC-CMAQ			41.70	-6.71	-13.86	19.91	0.66	0.81

821

822 The higher MDA8 O₃ in NACC-CMAQ degrades its regional NMB, NME, and R
 823 performance slightly compared to the prior NAQFC (Table 4), but R and IOA illustrate
 824 improvements for most regions, in some cases substantially for R (e.g., northeast, southeast,
 825 upper Midwest, and the Central Plains). The higher daytime O₃ overpredictions by NACC-
 826 CMAQ in much of CONUS result in higher NMB and NME values that fall outside of the Emery
 827 et al. (2017) benchmark criteria. These remain a concern for both the prior NAQFC and NACC-
 828 CMAQ, and efforts are underway to address the persistent daytime O₃ overprediction in the
 829 summer, particularly in the eastern U.S. (see Figures 14a-b and further discussion in Section 5).

830
 831
 832



833 **Table 4.** Same as in Table 3, but for MDA8 O₃. Note: As discussed in Emery et al. (2017),
 834 cutoff values are not applied for MDA8 O₃.

Day 1 Forecasts	Total # of Pairs	Mean Obs (ppb)	Mean Mod (ppb)	Mean Bias (ppb)	NMB (%)	NME (%)	Corr (r)	IOA
Benchmark Emery et al. (2017)	-	-	-	-	Goal: <±5% Criteria: <±15%	Goal: <15% Criteria: <25%	Goal: >0.75 Criteria: >0.50	-
Region 1 (Northeast)								
NAQFC	1680	33.05	38.45	5.40	16.35	22.60	0.66	0.73
NACC-CMAQ			38.60	5.55	16.81	21.57	0.73	0.75
Region 2 (NY-NJ)								
NAQFC	1158	32.79	37.07	4.29	13.08	21.38	0.66	0.76
NACC-CMAQ			39.22	6.44	19.63	23.65	0.74	0.75
Region 3 (Mid-Atlantic)								
NAQFC	4243	33.85	39.35	5.50	16.24	20.75	0.74	0.77
NACC-CMAQ			41.31	7.46	22.05	24.54	0.76	0.75
Region 4 (Southeast)								
NAQFC	5076	31.01	40.30	9.29	29.95	31.83	0.64	0.64
NACC-CMAQ			41.06	10.05	32.41	33.40	0.74	0.67
Region 5 (Upper Midwest)								
NAQFC	5210	34.08	37.88	3.80	11.16	18.51	0.75	0.82
NACC-CMAQ			39.89	5.81	17.06	19.94	0.82	0.82
Region 6 (South)								
NAQFC	3901	35.65	42.37	6.72	18.84	23.91	0.74	0.77
NACC-CMAQ			43.01	7.35	20.63	24.35	0.78	0.78
Region 7 (Central Plains)								



NAQFC	1256	33.37	37.83	4.46	13.36	17.99	0.78	0.82
NACC-CMAQ			39.36	6.00	17.97	19.86	0.85	0.84
Region 8 (Northern Plains)								
NAQFC	2379	44.18	43.51	-0.47	-1.07	12.84	0.74	0.85
NACC-CMAQ			44.95	0.78	1.76	11.78	0.79	0.88
Region 9 (West)								
NAQFC	5757	51.03	51.26	0.23	0.44	17.84	0.70	0.82
NACC-CMAQ			48.03	-3.00	-5.88	18.73	0.68	0.79
Region 10 (Northwest)								
NAQFC	698	33.13	35.46	2.33	7.03	25.11	0.63	0.72
NACC-CMAQ			36.66	3.53	10.67	25.58	0.59	0.74

835

836

837

There are substantial improvements in the overall statistical PM_{2.5} performance for

838 NACC-CMAQ, especially for R and IOA in most CONUS regions. In many regions where the

839 prior NAQFC falls outside of photochemical criteria values (Emery et al., 2017), NACC-CMAQ

840 shows significant improvement to fall within the criteria. This demonstrates a substantial

841 improvement in the accuracy of the NACC-CMAQ system for PM_{2.5} predictions (outside of

842 major wildfires), attributed to the scientific advancements described above.

843

844

845

846

847

848

849



850 **Table 5.** Same as in Table 3, but for 24-hr average PM_{2.5}. Note: As discussed in Emery et al.
 851 (2017), cutoff values are not applied for 24-hr average PM_{2.5}.

Day 1 Forecasts	Total # of Pairs	Mean Obs (ppb)	Mean Mod (ppb)	Mean Bias (ppb)	NMB (%)	NME (%)	Corr (r)	IOA
Benchmark Emery et al. (2017)	-	-	-	-	Goal: <±10% Criteria: <±30%	Goal: <35% Criteria: <50%	Goal: >0.70 Criteria: >0.40	-
Region 1 (Northeast)								
NAQFC	1261	7.43	8.47	1.04	13.98	42.57	0.77	0.85
NACC-CMAQ			9.39	1.95	26.30	46.17	0.75	0.83
Region 2 (NY-NJ)								
NAQFC	598	8.54	15.39	6.85	80.25	89.21	0.72	0.55
NACC-CMAQ			10.84	2.30	26.90	47.60	0.77	0.74
Region 3 (Mid-Atlantic)								
NAQFC	1897	9.16	11.95	2.79	30.43	42.57	0.81	0.84
NACC-CMAQ			10.16	1.00	10.96	33.24	0.83	0.89
Region 4 (Southeast)								
NAQFC	3621	8.45	9.67	1.23	14.53	40.44	0.41	0.62
NACC-CMAQ			7.86	-0.59	-6.98	37.19	0.48	0.67
Region 5 (Upper Midwest)								
NAQFC	3270	9.61	9.79	0.19	1.93	38.09	0.58	0.75
NACC-CMAQ			9.65	0.04	0.46	31.42	0.72	0.84
Region 6 (South)								
NAQFC	2101	8.39	7.95	-0.44	-5.19	46.68	0.28	0.57
NACC-CMAQ			6.39	-2.00	-23.82	43.30	0.36	0.59
Region 7 (Central Plains)								



NAQFC	926	8.67	9.83	1.16	13.41	49.67	0.32	0.58
NACC-CMAQ			8.79	0.12	1.40	32.13	0.68	0.82
Region 8 (Northern Plains)								
NAQFC	1790	7.66	4.36	-3.30	-43.13	60.51	0.33	0.55
NACC-CMAQ			4.89	-2.77	-36.20	52.68	0.49	0.67
Region 9 (West)								
NAQFC	4118	10.09	7.04	-3.05	-30.27	46.97	0.61	0.74
NACC-CMAQ			7.98	-2.11	-20.89	50.69	0.56	0.73
Region 10 (Northwest)								
NAQFC	3922	7.93	6.86	-1.07	-13.54	78.99	0.20	0.46
NACC-CMAQ			6.33	-1.60	-20.19	71.73	0.23	0.49

852
 853
 854

The Day 2 forecast comparisons of the prior NAQFC and NACC-CMAQ regional

855 statistics are similar to Day 1, and that the Day 3 forecast extension for NACC-CMAQ has utility
 856 with O₃ and PM_{2.5} statistics predominantly falling within the benchmark criteria in most regions
 857 (Tables S5-S10).

858 5. Conclusions and Path Forward

859 An advanced National Air Quality Forecasting Capability (NAQFC) was developed and
 860 evaluated, using NOAA's FV3-based Global Forecast System (GFS) as the driving meteorology
 861 for a state-of-the-science Community Multiscale Air Quality (CMAQ) model, version 5.3.1. A
 862 key component of this new system is the development of the NOAA-EPA Atmosphere
 863 Chemistry Coupler (NACC), which forms the bridge between the GFSv16 meteorological fields
 864 and the CMAQ inputs for improved chemical predictions (i.e., NACC-CMAQ). Such
 865 advancements of the NACC-CMAQ system include high-resolution satellite vegetation inputs,
 866 with a rapid-refresh VIIRS greenness vegetation fraction and VIIRS climatological leaf area



867 index, as well as additional soil data inputs to an improved windblown dust (FENGSHA)
868 algorithm in CMAQ. The anthropogenic, biogenic, and wildfire emissions in NACC-CMAQ are
869 also updated compared to the prior NAQFC, and for the first time, the forecasting model
870 calculates inline bidirectional NH_3 fluxes. NACC-CMAQ also ingests novel smoke and dust
871 aerosols at its lateral boundaries dynamically from the NOAA operational GEFS-Aerosols
872 model. Finally, the NACC-CMAQ system extends the air quality forecast from 48 to 72-hours,
873 and provides scientific advances in atmospheric chemistry modeling to state and local forecasters
874 out to 3 days. The additional day of forecast guidance could aid decision makers to prepare
875 citizens for localized air quality conditions that could adversely affect public health.

876 Results of the NACC-CMAQ system during recent late summer (September 2020) and
877 winter (January 2021) months show significant changes in both meteorological and chemical
878 predictions compared to the prior NAQFC. The GFSv16 for NACC-CMAQ has a persistently
879 large dry bias (lower Q2) and larger RMSE across much of CONUS in late summer compared to
880 NMMB (i.e., prior NAQFC), which likely stems from excessively dry soil conditions in GFS.
881 GFS is generally cooler in the east and warmer in the west for surface temperature (TEMP2)
882 compared to NMMB, but the overall MB and RMSE are more similar between the models
883 compared to that for Q2. The GFS has a relatively similar planetary boundary layer height
884 (PBLH) at night, but the PBLH in GFSv16 (NACC-CMAQ) is consistently deeper during the
885 daytime peak hours compared to the prior NAQFC. The differences in surface characteristics,
886 meteorology, and both anthropogenic and natural emissions are driving factors for distinct
887 atmospheric composition differences, where NACC-CMAQ generally outperforms the prior
888 NAQFC for both hourly O_3 and $\text{PM}_{2.5}$, especially with improved correlation (R) and IOA. This
889 agrees well with significant improvements in the diurnal O_3 and $\text{PM}_{2.5}$ patterns for NACC-



890 CMAQ, with distinct improvements in the day-to-night O₃ slope/cutoff. While overall similar,
891 the maximum daily 8-hr average (MDA8) O₃ is predominantly higher for NACC-CMAQ
892 compared to prior NAQFC, which leads to some forecast degradation due to larger
893 overpredictions of the daytime max O₃.

894 The NACC-CMAQ became the next operational version of the NAQFC at NWS/NOAA
895 on July 20, 2021, and is available on GitHub for continuous integration, future code updates, and
896 potential community research applications. Tang et al. (2021b) also shows the potential for
897 cloud applications of the operational GFSv16 data and NACC processing for community CMAQ
898 applications for any regional domain across the globe. A comparison and evaluation of the
899 GFSv16/NACC-CMAQ output with a GFSv16-downscaled Weather Research and Forecasting
900 (WRF) Version 4 (Skamarock et al., 2019) and CMAQ application serves to highlight the
901 potential of NACC-CMAQ as an additional community research tool for air quality applications
902 (Tang et al., 2021b).

903 While there are substantial advancements in NACC-CMAQ compared to the prior
904 NAQFC, challenges and limitations remain. One need is to bridge the gap from using a VIIRS
905 LAI climatology to a rapid-refresh, i.e., dynamic methodology (similar to the GVF method here)
906 in NACC-CMAQ. There is also a need to consider shifting the paradigm from using “big-leaf”
907 (i.e., homogeneous single layer of phytomass) assumptions that strongly affect the biosphere-
908 atmosphere exchange processes pivotal to both meteorological and chemical model predictions
909 (refer to Bonan et al., 2021). Simple multilayer canopies have shown to reduce overpredictions
910 of ground-level surface O₃ in the summer due to photolysis attenuation and modified vertical
911 turbulence (Makar et al., 2017), which have significant implications for the daytime O₃
912 overpredictions in the current and future versions of NAQFC (Figures 14a-b and S26). We are



913 currently working on similar canopy effects in NACC-CMAQ to reduce the summer O₃
914 overpredictions in the east-southeast and parts of western CONUS where there are relatively
915 continuous vegetation/canopies (Figures 14a-b). Other advancements that are important to
916 improving the future versions of the NAQFC include dynamically updated (and weather-
917 dependent) anthropogenic emissions sources, and improved treatments of mobile sources (e.g.,
918 Vehicle Induced Turbulence; Makar et al., 2021). Further refinements to the inline windblown
919 dust emissions, wildfire smoke emissions, and other process-based natural emissions sources are
920 also needed.

921 Other future directions including migrating the advanced science in the offline 12 km
922 resolution NACC-CMAQ model, to a next-generation inline, high-resolution (e.g., 3 km)
923 modeling framework that fits within NOAA's strategy for the Unified Forecast System (UFS;
924 <https://ufsccommunity.org/>). This model system aims to improve integration of atmospheric
925 composition changes with weather predictions, better resolve finer scale processes, and advance
926 the rapid-refresh techniques for emissions and surface-atmosphere exchange processes. The
927 advanced NACC-CMAQ system is an important step to advance the NAQFC closer to the state-
928 of-the-science for regional air quality forecasting, improves community applications of NOAA's
929 FV3GFS-driven atmospheric composition models, and facilitates future development of inline,
930 regional high-resolution air quality forecasting systems within the UFS framework.

931 **Code and Data Availability**

932 The NACC code is publicly available at <https://doi.org/10.5281/zenodo.5507489> and via
933 GitHub at <https://github.com/noaa-oar-arl/NACC.git>. The modified version of CMAQv5.3.1
934 used in the advanced NACC-CMAQ model for the next operational NAQFC is available at



935 <https://doi.org/10.5281/zenodo.5507511> and via GitHub at <https://github.com/noaa-oar->
936 [arl/NAQFC-WCOSS](#).

937 The 0.25 degree FV3-driven Global Forecast System Version 16 data (cycled 4x/day) is
938 available in GRIB2 format at <https://www.nco.ncep.noaa.gov/pmb/products/gfs/>. The hourly
939 GFSv16 data in gridded NetCDF (~13x13 km globally) format and Gaussian projection that is
940 directly used to drive NACC-CMAQ is currently being migrated to Amazon Web Services
941 (AWS) Cloud for community research applications, and is provided in more detail in Tang et al.
942 (2021b). The advanced NACC-CMAQ data, i.e., the current operational NAQFC version as of
943 July 2021, is available for operational (<https://airquality.weather.gov/>) and interactive
944 (<https://digital.mdl.nws.noaa.gov/airquality/#>) displays from NWS/NOAA. The official
945 NOAA/EMC verification and diagnostics for the NAQFC system are found at
946 https://www.emc.ncep.noaa.gov/mmb/aq/verification_diagnostics/cmaq_verf/.

947 **Disclaimer**

948 The scientific results and conclusions, as well as any views or opinions expressed herein,
949 are those of the author(s) and do not necessarily reflect the views of NOAA or the Department of
950 Commerce. The research presented was not funded by EPA and was not subject to EPA's quality
951 system requirements. The views expressed in this article are those of the author(s) and do not
952 necessarily represent the views or the policies of the U.S. Environmental Protection Agency.

953 **Author Contribution**

954 Patrick C. Campbell: Conceptualization, Methodology, Software, Data curation,
955 Visualization, Investigation, Writing – original draft. Youhua Tang: Methodology, Software,
956 Data curation, Investigation. Pius Lee: Supervision, Project administration, Funding acquisition.
957 Barry Baker: Methodology, Software, Data curation. Daniel Tong: Methodology, Software,



958 Writing – review & editing, Project administration, Funding acquisition. Rick Saylor:
959 Supervision, Project administration, Funding acquisition, Writing – review & editing. Ariel
960 Stein: Supervision, Project administration, Funding acquisition. Jianping Huang: Software, Data
961 curation. Ho-Chun Huang: Methodology, Software, Data curation. Jeff McQueen: Project
962 administration, Funding acquisition. Li Pan: Software, Data curation. Edward Strobach:
963 Software, Data curation, Writing – review & editing. Ivanka Stajner: Project administration,
964 Funding acquisition. James Sims: Project administration. Jose Tirado-Delgado: Project
965 administration. Youngsun Jung: Project administration, Funding acquisition. Fanglin Yang:
966 Project administration. Tanya Spero: Methodology, Software, Writing – review & editing.
967 Robert Gilliam: Software, Data curation.

968 **Declaration of competing interest**

969 The authors declare that they have no known competing financial interests or personal
970 relationships that could have appeared to influence the work reported in this paper.

971 **Acknowledgments**

972 This study was co-funded by the National Oceanic and Atmospheric Administration, the
973 University of Maryland, and George Mason University under the Cooperative Institute for
974 Satellite Earth System Studies (CISESS).



References

- Alexander, B., R.J. Park, D.J. Jacob, and S. Gong (2009), Transition metal-catalyzed oxidation of atmospheric sulfur: global implications for the sulfur budget, *J. Geophys. Res.*, 114, D02309, doi: 10.1029/2008JD010486.
- Aligo, E., , Ferrier B. S. , , Rogers E. , , Pyle M. , , Weiss S. J. , , and Jirak I. L. , 2014: Modified microphysics for use in high-resolution NAM forecasts. *Proc. 27th Conf. on Severe Local Storms*, Madison, WI, Amer. Meteor. Soc., 16A.1. [Available online at <https://ams.confex.com/ams/27SLS/webprogram/Paper255732.html>.]
- American Lung Association. Urban air pollution and health inequities: A workshop report. *Environ Health Perspect.* 2001; 109 (suppl 3): 357-374
- Appel, K. W., R.C. Gilliam, N. Davis, A. Zubrow, S.C. Howard Overview of the atmospheric model evaluation tool (amet) v1.1 for evaluating meteorological and air quality models *Environ. Model. Software*, 26 (2011), pp. 434-443, 10.1016/j.envsoft.2010.09.007
- Appel, K. W., Bash, J. O., Fahey, K. M., Foley, K. M., Gilliam, R. C., Hogrefe, C., Hutzell, W. T., Kang, D., Mathur, R., Murphy, B. N., Napelenok, S. L., Nolte, C. G., Pleim, J. E., Pouliot, G. A., Pye, H. O. T., Ran, L., Roselle, S. J., Sarwar, G., Schwede, D. B., Sidi, F. I., Spero, T. L., and Wong, D. C.: The Community Multiscale Air Quality (CMAQ) Model Versions 5.3 and 5.3.1: System Updates and Evaluation (2021), *Geosci. Model Dev. Discuss*, <https://doi.org/10.5194/gmd-14-2867-2021>.
- Astitha, M., H. Luo, S.T. Rao, C. Hogrefe, R. Mathur, N. Kumar Dynamic evaluation of two decades of WRF-CMAQ ozone simulations over the contiguous United States *Atmos. Environ.*, 164 (2017), pp. 102-116, 10.1016/j.atmosenv.2017.05.020
- Bai L, Wang J, Ma X, Lu H. Air Pollution Forecasts: An Overview. *Int J Environ Res Public Health*. 2018;15(4):780. Published 2018 Apr 17. doi:10.3390/ijerph15040780
- Baker, Barry; Pan, Li. 2017. "Overview of the Model and Observation Evaluation Toolkit (MONET) Version 1.0 for Evaluating Atmospheric Transport Models." *Atmosphere* 8, no. 11: 210. <https://doi.org/10.3390/atmos8110210>.
- Bash, J. O., J. T. Walker, G. G. Katul, M. R. Jones, E. Nemitz, and W. P. Robarge (2010), Estimation of In-Canopy Ammonia Sources and Sinks in a Fertilized *Zea mays* Field, *Environ. Sci. Technol.*, 44, 1683–1689, doi: 10.1021/es9037269.
- Bash, J. O., Cooter, E. J., Dennis, R. L., Walker, J. T., & Pleim, J. E. (2013). Evaluation of a regional air-quality model with bidirectional NH₃ exchange coupled to an agroecosystem model. *Biogeosciences*, 10(3), 1635–1645. <https://doi.org/10.5194/bg-10-1635-2013>
- Bash, J.O., Baker, K.R., Beaver, M.R., 2015, Evaluation of improved land use and canopy representation in BEIS v3.61 with biogenic VOC measurements in California, *Geosci. Model Dev. Discuss.* 8, 8117-8154, doi:10.5194/gmdd-8-8117-2015
- Binkowski, F. S., and Roselle S. J., 2003: Models-3 Community Multiscale Air Quality (CMAQ) model aerosol component 1. Model description. *J. Geophys. Res.*, 108, 4183, doi:10.1029/2001JD001409.



Binkowski, F.S., S. Arunachalam, Z. Adelman, and J. Pinto (2007), Examining photolysis rates with a prototype on-line photolysis module in CMAQ, *J. Appl. Meteor. and Clim.* 46, 1252-1256, doi: 10.1175/JAM2531.1.

Black, 1994 T. Black The new NMC meso-scale Eta Model: description and forecast examples *Weather and Forecasting*, 9 (1994), pp. 265-278

Bonan, G. B., E. G. Patton, J. J. Finnigan, D. D. Baldocchi, and I. N. Harman (2021). Moving beyond the incorrect but useful paradigm: reevaluating big-leaf and multilayer plant canopies to model biosphere-atmosphere fluxes – a review. *Agricultural and Forest Meteorology*. 306. <https://doi.org/10.1016/j.agrformet.2021.108435>.

Briggs, G. A., "A plume rise model compared with observations," *J.A.P.C.A.*, 15 (9), 433-438 (1965).

Byun and Ching, 1999 Byun, D.W., Ching, J.K.S., (Eds.), 1999. Science algorithms of the EPA Models-3 Community Multi-scale Air Quality (CMAQ) modeling system, EPA/600/R-99/030, Office of Research and Development, US Environmental Protection Agency.

Byun, D., & Schere, K. L. (2006). Review of the governing equations, computational algorithms, and other components of the models-3 community multiscale air quality (CMAQ) modeling system. *Applied Mechanics Reviews*, 59(1–6), 51–77. <https://doi.org/10.1115/1.2128636>

Campbell, G. S. and Norman, J. M.: An introduction to environmental biophysics, Springer, 5 1998

Campbell, P., Y. Zhang, K. Yahya, K. Wang, C. Hogrefe, G. Pouliot, C. Knote, A. Hodzic, R. San Jose, J. Perez, P. J. Guerrero, R. Baro, and P. Makar, 2015, A Multi-Model Assessment for the 2006 and 2010 Simulations under the Air Quality Model Evaluation International Initiative (AQMEII) Phase 2 over North America: Part I. Indicators of the Sensitivity of O₃ and PM_{2.5} Formation Regimes, *Atmospheric Environment*, 115, 569 – 586, doi: 10.1016/j.atmosenv.2014.12.026.

Campbell, P. C., Bash, J. O., & Spero, T. L. (2019). Updates to the Noah land surface model in WRF-CMAQ to improve simulated meteorology, air quality, and deposition. *Journal of Advances in Modeling Earth Systems*, 11, 231–256. <https://doi.org/10.1029/2018MS001422>

Campbell, P. C., Tong, D., Tang, Y., Baker, B., Lee, P., Saylor, R., Stein, A., Ma, S., Lamsal, L., and Qu, Z. (2021). Impacts of the COVID-19 Economic Slowdown on Ozone Pollution in the U.S. *Atmospheric Environment*, In press. Available online 4 September 2021, 118713

J.-H. Chen and S.-J. Lin. The remarkable predictability of inter-annual variability of atlantic hurricanes during the past decade. *Geophysical Research Letters*, 38(L11804):6, 2011.

J.-H. Chen and S.-J. Lin. Seasonal predictions of tropical cyclones using a 25-km-resolution general circulation model. *J. Climate*, 26(2):380–398, 2013.

Chen, F., & Dudhia, J. (2001). Coupling an advanced land surface-hydrology model with the Penn State-NCAR MM5 modeling system. Part I: Model implementation and sensitivity.



Monthly Weather Review, 129(4), 569–585. [https://doi.org/10.1175/1520-0493\(2001\)129<0569:CAALSH>2.0.CO;2](https://doi.org/10.1175/1520-0493(2001)129<0569:CAALSH>2.0.CO;2)

Chen, X., N. Andronova, B. Van Leer, J.E. Penner, J.P. Boyd, C. Jablonowski, and S. Lin, 2013: A Control-Volume Model of the Compressible Euler Equations with a Vertical Lagrangian Coordinate. *Mon. Wea. Rev.*, 141, 2526–2544, <https://doi.org/10.1175/MWR-D-12-00129.1>

Chen, Jan-Huey, Xi Chen, Shian-Jiann Lin, Linus Magnusson, Morris A. Bender, Linjiong Zhou and Shannon L. Rees. “TROPICAL CYCLONES IN GFDL FVGFS – IMPACTS OF DYCORE , PHYSICS , AND INITIAL CONDITIONS.” (2018).

Chen, X. et al. (2021). Evaluation of the offline-coupled GFSv15-FV3-CMAQv5.0.2 in support of the next-generation National Air Quality Forecast Capability over the contiguous United States. *GMD Discussion*. Under review.

Chin, M., P. Ginoux, S. Kinne, B. N. Holben, B. N. Duncan, R. V. Martin, J. A. Logan, A. Higurashi, and T. Nakajima, Tropospheric aerosol optical thickness from the GOCART model and comparisons with satellite and sun photometer measurements, *J. Atmos. Sci.* 59, 461-483, 2002.

Chin, M., R. B. Rood, S.-J. Lin, J. F. Muller, and A. M. Thomson, Atmospheric sulfur cycle in the global model GOCART: Model description and global properties, *J. Geophys. Res.*, 105, 24,671-24,687, 2000.

Chinese State Council, Air Pollution Prevention and Control Action Plan (Guo Fa [2013] No. 37, Sept. 10, 2013), http://www.gov.cn/zw/gk/2013-09/12/content_2486773.htm (in Chinese), archived at <https://perma.cc/63LS-QXDJ>; English translation at <http://en.cleairchina.org/file/loadFile/26.html>, archived at <https://perma.cc/S5FB-4ECZ>.

Clough, S. A., Shephard, M. W., Mlawer, J. E., Delamere, J. S., Iacono, M. J., Cady-Pereira, K., et al. (2005). Atmospheric radiative transfer modeling: A summary of the AER codes. *Journal of Quantitative Spectroscopy & Radiative Transfer*, 91(2), 233–244. <https://doi.org/10.1016/j.jqsrt.2004.05.058>

Cooter, E. J., Bash, J. O., Walker, J. T., Jones, M. R., & Robarge, W. (2010). Estimation of NH₃ bi-directional flux from managed agricultural soils. *Atmospheric Environment*, 44(17), 2107–2115. <https://doi.org/10.1016/j.atmosenv.2010.02.044>

Cooter, E. J., Bash, J. O., Benson, V., & Ran, L. (2012). Linking agricultural crop management and air quality models for regional to national-scale nitrogen assessments. *Biogeosciences*, 9(10), 4023–4035. <https://doi.org/10.5194/bg-9-4023-2012>

Demetriou, C. A., and Vineis, P. (2015). Carcinogenicity of ambient air pollution: use of biomarkers, lessons learnt and future directions.

Ding, H. and Y. Zhu (2018). NDE Vegetation Products System Algorithm Theoretical Basis Document. Version 4.0. NOAA/NESDIS/OSPO. Accessed on February 02, 2021. Available from: https://www.ospo.noaa.gov/Products/documents/GVF_ATBD_V4.0.pdf



- Dong, X., J. S. Fu, K. Huang, D. Tong, and G. Zhuang (2016). Model development of dust emission and heterogeneous chemistry within the Community Multiscale Air Quality modeling system and its application over East Asia. *Atmos. Chem. Phys.*, 16, 8157-8180.
- Driemel, A., Augustine, J., Behrens, K., Colle, S., Cox, C., Cuevas-Agulló, E., et al. (2018). Baseline Surface Radiation Network (BSRN): Structure and data description (1992–2017). *Earth System Science Data*, 10(3), 1491–1501. <https://doi.org/10.5194/essd-10-1491-2018>
- Eder, B., Kang, D., Mathur, R., Yu, S., & Schere, K. (2006). An operational evaluation of the Eta-CMAQ air quality forecast model. *Atmospheric Environment*, 40(26), 4894–4905. <https://doi.org/10.1016/j.atmosenv.2005.12.062>
- Eder, B., Kang, D., Mathur, R., Pleim, J., Yu, S., Otte, T., & Pouliot, G. (2009). A performance evaluation of the National Air Quality Forecast Capability for the summer of 2007. *Atmospheric Environment*, 43(14), 2312–2320. <https://doi.org/10.1016/j.atmosenv.2009.01.033>
- Ek, M. B., Mitchell, K. E., Lin, Y., Rogers, E., Grunmann, P., Koren, V., et al. (2003). Implementation of Noah land surface model advances in the National Centers for Environmental Prediction operational mesoscale Eta model. *Journal of Geophysical Research*, 108(D22), 8851. <https://doi.org/10.1029/2002JD003296>
- Emery, C., Zhen Liu, Armistead G. Russell, M. Talat Odman, Greg Yarwood & Naresh Kumar (2017). Recommendations on statistics and benchmarks to assess photochemical model performance, *Journal of the Air & Waste Management Association*, 67:5, 582-598, DOI: 10.1080/10962247.2016.1265027.
- Finkelstein et al. Relation between income, air pollution and mortality: A cohort study. *CMAJ*. 2003; 169: 397-402
- Ginoux, P., M. Chin, I. Tegen, J. Prospero, B. Holben, O. Dubovik, and S.-J. Lin, Sources and global distributions of dust aerosols simulated with the GOCART model, *J. Geophys. Res.*, 106, 20,255-20,273, 2001.
- Grell, G. A., Dudhia, J., & Stauffer, D. R. (1994). A description of the fifth-generation Penn State/NCAR Mesoscale Model (MM5). NCAR tech. Note NCAR TN-398-1-STR, 117 pp.
- Han, J. and H.-L. Pan, 2011: Revision of Convection and Vertical Diffusion Schemes in the NCEP Global Forecast System. *Wea. and Forecasting*, 26, 520-533.
- Han, J., W. Wang, Y. C. Kwon, S.-Y. Hong, V. Tallapragada, and F. Yang, 2017: Updates in the NCEP GFS Cumulus Convection Schemes with Scale and Aerosol Awareness. *Wea. and Forecasting*, 32, 2005-2017.
- Han, J., & Bretherton, C. S. (2019). TKE-Based Moist Eddy-Diffusivity Mass-Flux (EDMF) Parameterization for Vertical Turbulent Mixing, *Weather and Forecasting*, 34(4), 869-886.
- Harris, L.M. and S. Lin, 2013: A Two-Way Nested Global-Regional Dynamical Core on the Cubed-Sphere Grid. *Mon. Wea. Rev.*, 141, 283–306, <https://doi.org/10.1175/MWR-D-11-00201.1>



Harris, L.M., S. Lin, and C. Tu, 2016: High-Resolution Climate Simulations Using GFDL HiRAM with a Stretched Global Grid. *J. Climate*, 29, 4293–4314, <https://doi.org/10.1175/JCLI-D-15-0389.1>

Hengl, T., Mendes de Jesus, J., Heuvelink, G. B. M., Ruiperez Gonzalez, M., Kilibarda, M., Blagotić, A., Shangquan, W., Wright, M. N., Geng, X., Bauer-Marschallinger, B., Guevara, M. A., Vargas, R., MacMillan, R. A., Batjes, N. H., Leenaars, J. G. B., Ribeiro, E., Wheeler, I., Mantel, S., and Kempen, B.: SoilGrids250m: Global gridded soil information based on machine learning, *PLoS ONE*, 12, e0169748, <http://dx.doi.org/10.1371/journal.pone.0169748>, 2017b.
Huang, J., J. McQueen, J. Wilczak, I. Djalalova, I. Stajner, P. Shafran, D. Allured, P. Lee, L. Pan, D. Tong, H. Huang, G. DiMego, S. Upadhyay, and L. Delle Monache, 2017: Improving NOAA NAQFC PM2.5 Predictions with a Bias Correction Approach. *Wea. Forecasting*, 32, 407–421, <https://doi.org/10.1175/WAF-D-16-0118.1>

Huang, J., J. McQueen, et al., Impact of global scale FV3 versus regional scale NAM meteorological driver model predictions on regional air quality forecasting. The 100th AGU Fall Meeting, December 9-13, 2019, San Francisco, CA.

Huang, J., J. McQueen, et al., Development and evaluation of offline coupling of FV3-based GFS with CMAQ at NOAA, the 17th CMAS Conference, October 22-24, 2018, UNC-Chapel Hill, NC.

Huang, J., J. McQueen, et al., Development and evaluations of the GFS-driven National Air Quality Forecasting Capability at NOAA (in prep, to be submitted to GMD).

Huang, M., and Coauthors, 2015: Toward enhanced capability for detecting and predicting dust events in the western United States: The Arizona case study. *Atmos. Chem. Phys.*, 15, 12 595–12 610, doi:10.5194/acp-15-12595-2015.

Iacono, M. J., Delamere, J. S., Mlawer, E. J., Shephard, M. W., Clough, S. A., & Collins, W. D. (2008). Radiative forcing by long-lived greenhouse gases: Calculations with the AER radiative transfer models. *Journal of Geophysical Research*, 113, D13103. <https://doi.org/10.1029/2008JD009944>

Institute of Medicine. *Toward Environmental Justice: Research, Education, and Health Policy Needs*. Washington, DC: National Academy Press, 1999;

Janjić, Z. I., 2000: Comments on “Development and evaluation of a convection scheme for use in climate models.” *J. Atmos. Sci.*, 57, 3686, doi:10.1175/1520-0469(2000)057<3686:CODAEO>2.0.CO;2.

Janjić, Z. I., Gerrity J. P. Jr., and Nickovic S. (2001): An alternative approach to nonhydrostatic modeling. *Mon. Wea. Rev.*, 129, 1164–1178, doi:10.1175/1520-0493(2001)129<1164:AAATNM>2.0.CO;2.

Janjic, Z., & Gall, R. L. (2012). Scientific documentation of the NCEP nonhydrostatic multiscale model on the B grid (NMMB). Part 1 Dynamics (No. NCAR/TN-489+STR). University Corporation for Atmospheric Research. doi: 10.5065/D6WH2MZX.



- Jimenez, P. A., Dudhia, J., Gonzalez-Rouco, J. F., Navarro, J., Montavez, J. P., & Garcia-Bustamante, E. (2012). A revised scheme for the WRF surface layer formulation. *Monthly Weather Review*, 140(3), 898–918. <https://doi.org/10.1175/MWR-D-11-00056.1>
- Kang, Daiwen, Eder, B. K., Stein, A. F., Grell, G. A., Peckham, S. E., & Mc Henry, J. (2005). The New England Air Quality Forecasting Pilot Program: Development of an Evaluation Protocol and Performance Benchmark. *Journal of the Air and Waste Management Association*, 55(12), 1782–1796. <https://doi.org/10.1080/10473289.2005.10464775>
- Karamchandani, P., Long, Y., Pirovano, G., Balzarini, A., and Yarwood, G.: Source-sector contributions to European ozone and fine PM in 2010 using AQMEII modeling data, *Atmos. Chem. Phys.*, 17, 5643–5664, <https://doi.org/10.5194/acp-17-5643-2017>, 2017.
- Kar Kurt, O., Zhang, J., and Pinkerton, K. E. (2016) Pulmonary Health Effects of Air Pollution. *Curr Opin Pulm Med*, 22 (2), 138-143. doi:10.1097/MCP.0000000000000248
- Kelly, J. T., P. V. Bhave, C. G. Nolte, U. Shankar, and K. M. Foley (2010), Simulating emission and chemical evolution of coarse sea-salt particles in the Community Multiscale Air Quality (CMAQ) model, *Geosci. Model Dev.*, 3, 257–273, doi: 10.5194/gmd-3-257-2010.
- Kim, Y., Sartelet, K., Seigneur, C., 2011a. Formation of secondary aerosols: impact of the gas-phase chemical mechanism. *Atmos. Chem. Phys.* 11, 583e598. <http://dx.doi.org/10.5194/acp-11-583-2011>.
- Kim, Y., Couvidat, F., Sartelet, K., Seigneur, C., 2011b. Comparison of different gas phase mechanisms and aerosol modules for simulating particulate matter formation. *J. Air Waste Manag. Assoc.* 61, 1218e1226. <http://dx.doi.org/10.1080/10473289.2011.603999>.
- Keller, C. A. and Evans, M. J.: Application of random forest regression to the calculation of gas-phase chemistry within the GEOS-Chem chemistry model v10, *Geosci. Model Dev.*, 12, 1209–1225, <https://doi.org/10.5194/gmd-12-1209-2019>, 2019.
- S.K. Krueger, Q. Fu, K. N. Liou, and H-N. S. Chin. Improvement of an ice-phase microphysics parameterization for use in numerical simulations of tropical convection. *Journal of Applied Meteorology*, 34:281–287, January 1995.
- Landrigan, P. J., et al. (2018). The Lancet Commission on pollution and health. *Lancet* 2018; 391: 462-512. [http://dx.doi.org/10.1016/S0140-6736\(17\)32345-0](http://dx.doi.org/10.1016/S0140-6736(17)32345-0)
- Lee, B.-J., Kim, B., and Lee, K. (2014). Air Pollution Exposure and Cardiovascular Disease. *Toxicol Res.*, 30(2), 71-75.
- Lee, P., McQueen, J., Stajner, I., Huang, J., Pan, L., Tong, D., et al. (2017). NAQFC Developmental Forecast Guidance for Fine Particulate Matter (PM 2.5). *Weather and Forecasting*, 32(1), 343–360. <https://doi.org/10.1175/waf-d-15-0163.1>
- Lin, S., 2004: A “Vertically Lagrangian” Finite-Volume Dynamical Core for Global Models. *Mon. Wea. Rev.*, 132, 2293–2307, [https://doi.org/10.1175/1520-0493\(2004\)132<2293:AVLFDC>2.0.CO;2](https://doi.org/10.1175/1520-0493(2004)132<2293:AVLFDC>2.0.CO;2)



Lin, S. and R.B. Rood, 1996: Multidimensional Flux-Form Semi-Lagrangian Transport Schemes. *Mon. Wea. Rev.*, 124, 2046–2070, [https://doi.org/10.1175/1520-0493\(1996\)124<2046:MFFSLT>2.0.CO;2](https://doi.org/10.1175/1520-0493(1996)124<2046:MFFSLT>2.0.CO;2)

Y.-L. Lin, R. D. Farley, and H. D. Orville. Bulk parameterization of the snow field in a cloud model. *J. Climate Appl. Meteor.*, 22:1065–1092, 1983.

Lin, S., W.C. Chao, Y.C. Sud, and G.K. Walker, 1994: A Class of the van Leer-type Transport Schemes and Its Application to the Moisture Transport in a General Circulation Model. *Mon. Wea. Rev.*, 122, 1575–1593, [https://doi.org/10.1175/1520-0493\(1994\)122<1575:ACOTVL>2.0.CO;2](https://doi.org/10.1175/1520-0493(1994)122<1575:ACOTVL>2.0.CO;2)

Liu, Y. and Wang, T.: Worsening urban ozone pollution in China from 2013 to 2017 – Part 1: The complex and varying roles of meteorology, *Atmos. Chem. Phys.*, 20, 6305–6321, <https://doi.org/10.5194/acp-20-6305-2020>, 2020.

S.J. Lord, H.E. Willoughby, and J.M. Piotrowicz. Role of a parameterized ice-phase microphysics in an axisymmetric, nonhydrostatic tropical cyclone model. *J. Atmos. Sci.*, 41(19):2836–2848, October 1984.

Makar, P., Staebler, R., Akingunola, A. et al. The effects of forest canopy shading and turbulence on boundary layer ozone. *Nat Commun* 8, 15243 (2017). <https://doi.org/10.1038/ncomms15243>

Makar, P. A., Stroud, C., Akingunola, A., Zhang, J., Ren, S., Cheung, P., and Zheng, Q.: Vehicle-induced turbulence and atmospheric pollution, *Atmos. Chem. Phys.*, 21, 12291–12316, <https://doi.org/10.5194/acp-21-12291-2021>, 2021

Marlier, M.E., Jina, A.S., Kinney, P.L. et al. Extreme Air Pollution in Global Megacities. *Curr Clim Change Rep* 2, 15–27 (2016). <https://doi.org/10.1007/s40641-016-0032-z>

Martin, R. L. and T.W. Good (1991), Catalyzed oxidation of sulfur dioxide in solution: the iron-manganese synergism, *Atmospheric Environment*, 25A, 2395-2399, doi: 10.1016/0960-1686(91)90113-L.

Massad, R.-S., E. Nemitz, and M. A. Sutton (2010), Review and parameterization of bi-directional ammonia exchange between vegetation and the atmosphere, *Atmos. Chem. Phys.*, 10, 10359-10386, doi: 10.5194/acp-10-10359-2010.

Mathur, R., Yu, S., Kang, D., & Schere, K. L. (2008). Assessment of the wintertime performance of developmental particulate matter forecasts with the Eta-Community Multiscale Air Quality modeling system. *Journal of Geophysical Research*, 113(D2), D02303. <https://doi.org/10.1029/2007JD008580>

Matthias, V., Jan A. Arndt, Armin Aulinger, Johannes Bieser, Hugo Denier van der Gon, Richard Kranenburg, Jeroen Kuenen, Daniel Neumann, George Pouliot & Markus Quanté (2018) Modeling emissions for three-dimensional atmospheric chemistry transport models, *Journal of the Air & Waste Management Association*, 68:8, 763-800, DOI: 10.1080/10962247.2018.1424057

McKeen, S., Wilczak, J., Grell, G., Djalova, I., Peckham, S., Hsie, E.-Y., Gong, W., Bouchet, V., Ménard, S., Moffet, R., McHenry, J., McQueen, J., Tang, Y., Carmichael, G.R., Pagowski, M., Chan, A., Dye, t., Frost, G., Lee, P., Mathur, R.,



2005. Assessment of an ensemble of seven real-time ozone forecasts over eastern North America during the summer of 2004. *J. Geophys. Res.* 110, D21307. <http://dx.doi.org/10.1029/2005JD005858>.

McKeen, S., Chung, S.H., Wilczak, J., Grell, G., Djalalova, I., Peckham, S., Gong, W., Bouchet, V., Moffet, R., Tang, Y., Carmichael, G.R., Mathur, R., Yu, S., 2007. Evaluation of several PM_{2.5} forecast models using data collected during the ICARTT/NEAQS 2004 field study. *J. Geophys. Res.* 112, D10S20. <http://dx.doi.org/10.1029/2006JD007608>.

McKeen, S., et al., 2009. An evaluation of real-time air quality forecasts and their urban emissions over eastern Texas during the summer of 2006 Second Texas Air Quality Study field study. *J. Geophys. Res.* 114, D00F11. <http://dx.doi.org/10.1029/2008JD011697>.

Miller J, Safford H, Crimmins M, Thode A (2009) Quantitative evidence for increasing forest fire severity in the Sierra Nevada and Southern Cascade Mountains, California and Nevada, USA. *Ecosystems* 12:16–32

Mlawer, E. J., , Taubman S. J. , , Brown P. D. , , Iacono M. J. , , and Clough S. A. , 1997: Radiative transfer for inhomogeneous atmosphere: RTTM, a validated correlated-k model for the longwave. *J. Geophys. Res.*, 102, 16 663–16 682, doi:10.1029/97JD00237.

Monin, A. S., & Obukhov, A. M. (1954). Basic laws of turbulent mixing in the surface layer of the atmosphere (in Russian). Contribution Geophysics Institute, Academy of Sciences USSR, 151, 163–187.

Myneni, R., Knyazikhin, Y. (2018). VIIRS/NPP Leaf Area Index/FPAR 8-Day L4 Global 500m SIN Grid V001 [Data set]. NASA EOSDIS Land Processes DAAC. Accessed 2021-02-22 from <https://doi.org/10.5067/VIIRS/VNP15A2H.001>

National Emissions Inventory (NEI). (2014). Retrieved February 26, 2020, from https://edap.epa.gov/public/extensions/nei_report_2014/dashboard.html#sector-db

National Emissions Inventory Collaborative (2019). 2016v1 Emissions Modeling Platform. Retrieved from <http://views.cira.colostate.edu/wiki/wiki/10202>.

Nemitz, E., Sutton, M. A., Schjoerring, J. K., Husted, S., & Wyers, G. P. (2000). Resistance modelling of ammonia exchange over oilseed rape. *Agricultural and Forest Meteorology*, 105(4), 405–425. [https://doi.org/10.1016/S0168-1923\(00\)00206-9](https://doi.org/10.1016/S0168-1923(00)00206-9)

Niinemets, Ü., Arneth, A., Kuhn, U., Monson, R. K., Peñuelas, J., and Staudt, M.: The emission factor of volatile isoprenoids: stress, acclimation, and developmental responses, *Biogeosciences*, 7, 2203–2223, doi:10.5194/bg-7-2203-2010, 2010.



O'Neill MS, , et al. Health, wealth, and air pollution: Advancing theory and methods. *Environ Health Perspect.* 2003; 111: 1861-1870

O'Neill, S. M., and Coauthors, 2009: Regional real-time smoke prediction systems. *Wildland Fires and Air Pollution*, A. Bytnerowicz et al., Eds., *Developments in Environmental Science*, Vol. 8, Elsevier, 499–534.

Otte, T. L. and Pleim, J. E.: The Meteorology-Chemistry Interface Processor (MCIP) for the CMAQ modeling system: updates through MCIPv3.4.1, *Geosci. Model Dev.*, 3, 243–256, <https://doi.org/10.5194/gmd-3-243-2010>, 2010.

Otte, T. L., Pouliot, G., Pleim, J. E., Young, J. O., Schere, K. L., Wong, D. C., et al. (2005). Linking the Eta Model with the Community Multiscale Air Quality (CMAQ) Modeling System to Build a National Air Quality Forecasting System. *Weather and Forecasting*, 20(3), 367–384. <https://doi.org/10.1175/WAF855.1>

Pan, L., Kim, H., Lee, P., Saylor, R., Tang, Y., Tong, D., Baker, B., Kondragunta, S., Xu, C., Ruminski, M. G., Chen, W., McQueen, J., and Stajner, I.: Evaluating a fire smoke simulation algorithm in the National Air Quality Forecast Capability (NAQFC) by using multiple observation data sets during the Southeast Nexus (SENEX) field campaign, *Geosci. Model Dev.*, 13, 2169–2184, <https://doi.org/10.5194/gmd-13-2169-2020>, 2020.

Pinder, R.W., Dennis, R.L., Bhawe, P.V., 2008. Observable indicators of the sensitivity of PM_{2.5} nitrate to emission reductions: part I. Derivation of the adjusted gas ratio and applicability at regulatory-relevant time scales. *Atmos. Environ.* 42 (6), 1275e1286.

Pleim, J. E., 2007a: A combined local and nonlocal closure model for the atmospheric boundary layer. Part I: Model description and testing. *J. Appl. Meteor. Climatol.*, 46, 1383–1395, doi:10.1175/JAM2539.1.

Pleim, J. E., 2007b: A combined local and nonlocal closure model for the atmospheric boundary layer. Part II: Application and evaluation in a mesoscale meteorological model. *J. Appl. Meteor. Climatol.*, 46, 1396–1409, doi:10.1175/JAM2534.1.

Pleim, J., & Ran, L. (2011). Surface flux modeling for air quality applications. *Atmosphere*, 2(3), 271–302. <https://doi.org/10.3390/atmos2030271>.

Pleim, J. E., Bash, J. O., Walker, J. T., & Cooter, E. J. (2013). Development and evaluation of an ammonia bidirectional flux parameterization for air quality models. *Journal of Geophysical Research: Atmospheres*, 118, 3794–3806. <https://doi.org/10.1002/jgrd.50262>

Pleim, J. E., Ran, L., Appel, W., Shephard, M. W., & Cady-Pereira, K. (2019). New bidirectional ammonia flux model in an air quality model coupled with an agricultural model. *Journal of Advances in Modeling Earth Systems*, 11, 2934– 2957. <https://doi.org/10.1029/2019MS001728>



- Powers, J. G., Klemp, J. B., Skamarock, W. C., Davis, C. A., Dudhia, J., Gill, D. O., et al. (2017). The weather research and forecasting model: Overview, system efforts, and future directions. *Bulletin of the American Meteorological Society*, 98(8), 1717–1737. <https://doi.org/10.1175/BAMS-D-15-00308.1>
- Putman, W. M., and S.-J. Lin (2007). Finite-volume transport on various cubed-sphere grids, *Journal of Computational Physics*, 227, 1, 10, 55-78. <https://doi.org/10.1016/j.jcp.2007.07.022>
- Pye, H. O. T., R. W. Pinder, I. Piletic, Y. Xie, S. L. Capps, Y.-H. Lin, J. D. Surratt, Z. Zhang, A. Gold, D. J. Luecken, W. T. Hutzell, M. Jaoui, J. H. Offenberg, T. E. Kleindienst, M. Lewandowski, and E. O. Edney, Epoxide pathways improve model predictions of isoprene markers and reveal key role of acidity in aerosol formation, *Environmental Science & Technology*, <https://doi.org/10.1021/es402106h>, 2013.
- Pye, H. O. T., Murphy, B. N., Xu, L., Ng, N. L., Carlton, A. G., Guo, H., Weber, R., Vasilakos, P., Appel, K. W., Budisulistiorini, S. H., Surratt, J. D., Nenes, A., Hu, W., Jimenez, J. L., Isaacman-VanWertz, G., Misztal, P. K., and Goldstein, A. H.: On the implications of aerosol liquid water and phase separation for organic aerosol mass, *Atmospheric Chemistry and Physics*, 17, 343-369, <https://doi.org/10.5194/acp-17-343-2017>, 2017.
- Ran, L., Cooter, E., Benson, V., & He, Q. (2011). Development of an agricultural fertilizer modeling system for bi-directional ammonia fluxes in the CMAQ model. In D. G. Steyn, & S. T. Castelli (Eds.), *Air Pollution Modeling and its Application XXI* (Chapter 36, (pp. 213–219). Dordrecht: Springer. https://doi.org/10.1007/978-94-007-1359-8_36
- Ran, L., J. Pleim, R. Gilliam, F. S. Binkowski, C. Hogrefe, and L. Band (2016), Improved meteorology from an updated WRF/CMAQ modeling system with MODIS vegetation and albedo, *J. Geophys. Res. Atmos.*, 121, 2393– 2415, doi:10.1002/2015JD024406.
- Rogers et al., 1996 E. Rogers, T. Black, D. Deaven, G. DiMego, Q. Zhao, M. Baldwin, N. Junker, Y. Lin Changes to the operational “early” Eta Analysis/Forecast System at the National Centers for Environmental Prediction Weather and Forecasting, 11 (1996), pp. 391-413
- Ruminski, M. and Kondragunta, S.: Monitoring fire and smoke emissions with the hazard mapping system – art. no. 64120B. in: *Disaster Forewarning Diagnostic Methods and Management*, edited by: Kogan, F., Habib, S., Hegde, V. S., and Matsuoka, M., 2006.
- Ruminski, M., Simko, J., Kibler, J., Kondragunta, S., Draxler, R., Davidson, P., and Li, P.: Use of multiple satellite sensors in NOAA's operational near real-time fire and smoke detection and characterization program, in: *Remote Sensing of Fire: Science and Application*, edited by: Hao, W. M., 2008.
- Sarwar, G., K. Fahey, S. Napelenok, S. Roselle, and R. Mathur (2011), Examining the impact of CMAQ model updates on aerosol sulfate predictions, the 10th Annual CMAS Models-3 User's Conference, October, Chapel Hill, NC.



Sarwar, G., B. Gantt, K. Foley, K. Fahey, T. L. Spero, D. Kang, R. Mathur, H. Foroutan, J. Xing, T. Sherwen, A. Saiz-Lopez (2019). Influence of bromine and iodine chemistry on annual, seasonal, diurnal, and background ozone: CMAQ simulations over the Northern Hemisphere. *Atmospheric Environment*. 213. 395-404. <https://doi.org/10.1016/j.atmosenv.2019.06.020>.

Schwede, D., G. A. Pouliot, and T. Pierce (2005), Changes to the Biogenic Emissions Inventory System Version 3 (BEIS3), In Proceedings of the 4th CMAS Models-3 Users' Conference, Chapel Hill, NC, 26–28 September 2005.

Schroeder, W., Ruminski, M., Csiszar, I., Giglio, L., Prins, E., Schmidt, C., and Morissette, J.: Validation analyses of an operational fire monitoring product: The Hazard Mapping System, *Int. J. Remote Sens.*, 29, 6059–6066, <https://doi.org/10.1080/01431160802235845>, 2008.

Sillman, S., Logan, J. A. & Wofsy, S. C. The sensitivity of ozone to nitrogen oxides and hydrocarbons in regional ozone episodes. *J. Geophys. Res.* 95, 1837–1852 (1990).
Sillman, S. The use of NO_y, H₂O₂, and HNO₃ as indicators for ozone-NO_x-hydrocarbon sensitivity in urban locations. *J. Geophys. Res. Atmos.* 100, 14175–14188 (1995).
Sillman, S., The relation between ozone, NO_x and hydrocarbons in urban and polluted rural environments. *Millennial Review series, Atmos. Environ.*, 33, 12, 1821-1845, 1999.

Skamarock, W. C., & Klemp, J. B. (2008). A time-split nonhydrostatic atmospheric model for weather research and forecasting applications. *Journal of Computational Physics*, 227(7), 3465–3485. <https://doi.org/10.1016/j.jcp.2007.01.037>

Skamarock, W. C., Klemp, J. B., Dudhia, J., Gill, D. O., Liu, Z., Berner, J., Huang, X. -yu. (2019). A Description of the Advanced Research WRF Model Version 4 (No. NCAR/TN-556+STR). doi:10.5065/1dfh-6p97

Sofiev, M., Ermakova, T., and Vankevich, R.: Evaluation of the smoke-injection height from wild-land fires using remote-sensing data, *Atmos. Chem. Phys.*, 12, 1995–2006, <https://doi.org/10.5194/acp-12-1995-2012>, 2012.

Stajner, I., Davidson, P., Byun, D., McQueen, J., Draxler, R., Dickerson, P., & Meagher, J. (2011). US National Air Quality Forecast Capability: Expanding Coverage to Include Particulate Matter (pp. 379–384). Springer, Dordrecht. https://doi.org/10.1007/978-94-007-1359-8_64

Jian Sun, Joshua S. Fu, Kan Huang & Yang Gao (2015) Estimation of future PM_{2.5}- and ozone-related mortality over the continental United States in a changing climate: An application of high-resolution dynamical downscaling technique, *Journal of the Air & Waste Management Association*, 65:5, 611-623, DOI: 10.1080/10962247.2015.1033068

Tang, Youhua & Lee, Pius & Tsidulko, Marina & Huang, Ho-Chun & Mcqueen, Jeffery & DiMego, Geoffrey & Emmons, Louisa & Pierce, Robert & Thompson, Anne & Lin, Hsin-Mu & Kang, Daiwen & Tong, Daniel & Yu, Shaocai & Mathur, Rohit & Pleim, Jonathan & Otte, Tanya & Pouliot, George & Young, Jeffrey & Schere, Kenneth & Stajner, Ivanka. (2009). The impact of chemical lateral boundary conditions on CMAQ predictions of tropospheric ozone



over the continental United States. *Environmental Fluid Mechanics*. 9. 43-58. 10.1007/s10652-008-9092-5.

Tang, Y., Tianfeng Chai, Li Pan, Pius Lee, Daniel Tong, Hyun-Cheol Kim & Weiwei Chen (2015) Using optimal interpolation to assimilate surface measurements and satellite AOD for ozone and PM_{2.5}: A case study for July 2011, *Journal of the Air & Waste Management Association*, 65:10, 1206-1216, DOI: 10.1080/10962247.2015.1062439

Tang, Y., Bian, H., Tao, Z., Oman, L. D., Tong, D., Lee, P., Campbell, P. C., Baker, B., Lu, C.-H., Pan, L., Wang, J., McQueen, J., and Stajner, I.: Comparison of chemical lateral boundary conditions for air quality predictions over the contiguous United States during pollutant intrusion events, *Atmos. Chem. Phys.*, 21, 2527–2550, <https://doi.org/10.5194/acp-21-2527-2021>, 2021a.

Tang Y., P. C. Campbell, P. Lee, B. Baker, D. Tong, R. Saylor, A. Stein, F. Yang, J. Huang, H.-C. Huang, J. McQueen, I. Stajner, J. Sims, J. Tirado-Delgado, Y. Jung, F. Yang, and T. Spero (2021b). Evaluations and Community Applications in the Advanced National Air Quality Forecast Capability Using the NOAA Global Forecast System Version 16, GMD, In Prep.

Tewari, M., Chen, F., Wang, W., Dudhia, J., LeMone, M. A., Mitchell, K., et al. (2004). Implementation and verification of the unified NOAA land surface model in the WRF model. Paper Presented at the 20th Conference on Weather Analysis and Forecasting/16th Conference on Numerical Weather Prediction, Seattle, WA.

Tong, D.Q., P. Lee, and R.D. Saylor (2012). New Direction: The need to develop process-based emission forecasting models, *Atmospheric Environment*, 47: 560-561

Tong, D. Q., Wang, J. X. L., Gill, T. E., Lei, H., and Wang, B. (2017), Intensified dust storm activity and Valley fever infection in the southwestern United States, *Geophys. Res. Lett.*, 44, 4304–4312, doi:10.1002/2017GL073524.

Troen, I. and L. Mahrt, 1986: A simple model of the atmospheric boundary layer: Sensitivity to surface evaporation. *Bound.-Layer Meteor.*, 37, 129–148.

US EPA Office of Research and Development. (2014, May 30). CMAQv5.0.2 (Version 5.0.2). Zenodo. <http://doi.org/10.5281/zenodo.1079898>

US EPA Office of Research and Development. (2019, December 19). CMAQ (Version 5.3.1). Zenodo. <http://doi.org/10.5281/zenodo.3585898>

Vukovich, J. M., and T. Pierce (2002). The Implementation of BEIS3 within the SMOKE modeling framework.

Weiss, A. and Norman, J.: Partitioning solar radiation into direct and diffuse, visible and nearinfrared components, *Agr. Forest Meteorol.*, 34, 205–213, 1985.

Westerling AL, Hidalgo HG, Cayan DR, Swetnam TW (2006) Warming and earlier spring increase western US forest wildfire activity. *Science* 313:940–943.

Wilkins, J., G. Pouliot, T. Pierce, AND J. Beidler. Exploring the Vertical Distribution of Wildland Fire Smoke in CMAQ (2019 IEIC). 2019 International Emissions Inventory Conference, Dallas, Texas, July 28 - August 02, 2019.



- Williams, J. R. (1995). The EPIC model. In V. P. Singh (Ed.), *Computer models in watershed hydrology* (Chapter 25, (pp. 909–1000). Littleton, CO: Water Resources Publications.
- Williams, A. P., Cook, E. R., Smerdon, J. E., Cook, B. I., Abatzoglou, J. T., Bolles, K., Baek, S. H., Badger, A. M., Livneh, B. (2020). Large contribution from anthropogenic warming to an emerging North American megadrought. *Science*. 368, 314-318. DOI: 10.1126/science.aaz9600.
- World Health Organization (WHO), 2006. *Air Quality Guidelines. Global update 2005. Particulate matter, ozone, nitrogen dioxide and sulfur dioxide.*
- World Health Organization (WHO), 2010. *WHO Guidelines for Indoor Air Quality: Selected Pollutants.* World Health Organization, Regional Office for Europe Scherfigsvej 8, DK-2100 Copenhagen Ø, Denmark, ISBN 9789289002134.
- Yang, F., Tallapragada, V., Kain, J. S., Wei, H., Yang, R., Yudin, V. A., Moorthi, S., Han, J., Hou, Y. T., Wang, J., Treadon, R., and Kleist, D. T. (2020). Model Upgrade Plan and Initial Results from a Prototype NCEP Global Forecast System Version 16. 2020 AMS Conference, Boston, MA. <https://ams.confex.com/ams/2020Annual/webprogram/Paper362797.html>
- Yarwood, G., Rao S., Yocke M., and Whitten G., 2005: Updates to the carbon bond chemical mechanism: CB05. Final Rep. to the US EPA, RT-0400675. [Available online at http://www.camx.com/publ/pdfs/cb05_final_report_120805.pdf.]
- Yarwood, G., G. Z. Whitten, and J. Jung (2010). Final Report. Development, Evaluation and Testing of Version 6 of the Carbon Bond Chemical Mechanism (CB6). ENVIRON International Corporation. 06-17477Y. September 22, 2010.
- Zeka A, Zanobetti A, Schwartz J. Short term effects of particulate matter on cause specific mortality: effects of lags and modification by city characteristics. *Occup Environ Med*. 2006; 62: 718-725
- Zhang, X., Kondragunta, S., Ram, J., Schmidt, C., & Huang, H.-C. (2012). Near-real-time global biomass burning emissions product from geostationary satellite constellation. *Journal of Geophysical Research: Atmospheres*, 117(D14). <https://doi.org/10.1029/2012JD017459>
- Zhang, X., Kondragunta, S., & Roy, D. P. (2014). Interannual variation in biomass burning and fire seasonality derived from geostationary satellite data across the contiguous United States from 1995 to 2011. *Journal of Geophysical Research: Biogeosciences*, 119(6), 1147–1162. <https://doi.org/10.1002/2013JG002518>.
- Zhang, Y., Vijayaraghavan, K., Wen, X.-Y., Snell, H.E., Jacobson, M.Z., 2009a. Probing into regional ozone and particulate matter pollution in the United States: 1. A 1 year CMAQ simulation and evaluation using surface and satellite data. *J. Geophys. Res.* 114, D22304.
- Zhang, Y., Wen, X.-Y., Wang, K., Vijayaraghavan, K., Jacobson, M.Z., 2009b. Probing into regional ozone and particulate matter pollution in the United States: 2. An examination of formation mechanisms through a process analysis technique and sensitivity study. *J. Geophys. Res.* 114.



Zhang, Y., Bocquet, M., Mallet, V., Seigneur, C., and Baklanov, A. (2012a), Real-time air quality forecasting, part I: History, techniques, and current status. *Atmospheric Environment*. 60, 632-655.

Zhang, Y., Bocquet, M., Mallet, V., Seigneur, C., and Baklanov, A. (2012b), Real-time air quality forecasting, part II: State of the science, current research needs, and future prospects. *Atmospheric Environment*. 60, 656-676.

Zhang, Y., West, J. J., Mathur, R., Xing, J., Hogrefe, C., Roselle, S. J., Bash, J. O., Pleim, J. E., Gan, C.-M., and Wong, D. C.: Long-term trends in the ambient PM_{2.5}- and O₃-related mortality burdens in the United States under emission reductions from 1990 to 2010, *Atmos. Chem. Phys.*, 18, 15003–15016, <https://doi.org/10.5194/acp-18-15003-2018>, 2018.

Zhao, H.; Zheng, Y.; Li, T. Air Quality and Control Measures Evaluation during the 2014 Youth Olympic Games in Nanjing and its Surrounding Cities. *Atmosphere* 2017, 8, 100.

Zhou, L., S. Lin, J. Chen, L.M. Harris, X. Chen, and S.L. Rees, 2019: Toward Convective-Scale Prediction within the Next Generation Global Prediction System. *Bull. Amer. Meteor. Soc.*, 100, 1225–1243, <https://doi.org/10.1175/BAMS-D-17-0246.1>

Zhou, T.; Sun, J.; Yu, H. Temporal and Spatial Patterns of China's Main Air Pollutants: Years 2014 and 2015. *Atmosphere* 2017, 8, 137.